TRIBHUVAN UNIVERSITY
INSTITUTE OF ENGINEERING
PULCHOWK CAMPUS

THESIS NO: M-94-MSMDE-2023-2025

Hydrodynamic Forces and their Effects on Structural Design of Vertical Lift Gate

by
Ranjeet Twayna

A THESIS
SUBMITTED TO THE DEPARTMENT OF MECHANICAL AND AEROSPACE ENGINEERING IN PARTIAL FULFILLMENT OF THE REQUIREMENTS FOR THE DEGREE OF MASTERS OF SCIENCE IN MECHANICAL SYSTEMS DESIGN AND ENGINEERING

DEPARTMENT OF MECHANICAL AND AEROSPACE ENGINEERING
LALITPUR, NEPAL

April, 2025

COPYRIGHT

TRIBHUVAN UNIVERSITY

INSTITUTE OF ENGINEERING

PULCHOWK CAMPUS

DEPARTMENT OF MECHANICAL AND AEROSPACE ENGINEERING

The undersigned certify that they have read, and recommended to the Institute of Engineering for acceptance, a Final Thesis Report entitled "Hydrodynamic Forces and their Effect on Structural Design of Vertical Lift Gate" submitted by Ranjeet Twayna in partial fulfillment of the requirements for the degree of Master of Science in Mechanical System Design and Engineering.

Prof. Dr. Laxman Poudel
Supervisor,
Department of Mechanical and Aerospace Engineering

Nabin Kumar Shrestha
External Examiner,
CEO, Precise Hydro Engineering & Construction Pvt. Ltd.
Tripureshwor, Kathmandu

Asst. Prof. Sudip Bhattarai, PhD
Committee Chairperson,
Head of Department,
Department of Mechanical and Aerospace Engineering,

Date: April 07, 2025

ABSTRACT

Vertical lift gates are essential in hydraulic structures such as dams and flood control systems, regulating water flow. However, the complex hydrodynamic forces acting on these gates, particularly when partially open, cause significant design challenges. This study conducts hydrodynamic and structural analysis of vertical lift gates using Computational Fluid Dynamics (CFD) and Finite Element Analysis (FEA) to assess gate performance under various conditions. The methodology involves 2D and 3D modeling, meshing, and numerical simulations, followed by CFD analysis in ANSYS-FLUENT to examine hydrodynamic forces, validated against analytical calculations. FEA is used to assess the structural response under these forces. Results show that downpull peaks at 30% gate opening, reaching 48.41 kN (CFD) and 44.09 kN (Analytical). The force rises rapidly from 10% to 30%, stabilizes until 40%, and then declines, dropping to 10–15 kN at 80% opening. Strong agreement between CFD and analytical methods validates numerical predictions. FEA analysis reveals that incorporating downpull significantly increases stress and deformation levels, with maximum principal stress rising from 132.68 MPa to 180.68 MPa and equivalent (Von Mises) stress increasing by 27.5%. Stress concentrations remained localized at geometric discontinuities without indicating immediate failure risks. The end vertical girder consistently exhibited higher load demands than the main horizontal beams, highlighting its critical structural role. Transient analysis showed damped oscillatory deformation behavior, with slightly elevated peak deformations under downpull. These findings underline the necessity of considering downpull in gate design to enhance structural integrity and operational reliability.

ACKNOWLEDGEMENT

I would like to express my sincere gratitude to the individuals and organizations whose support has been instrumental in the completion of this thesis.

Supervisor: I am deeply grateful to my thesis supervisor, Professor Dr. Laxman Poudel of the Department of Mechanical and Aerospace Engineering at Pulchowk Campus, for his invaluable guidance, unwavering support, and insightful feedback throughout this research. His expertise and encouragement have been essential in shaping the direction of this study.

Friends: A heartfelt thank you to my friends for their constant encouragement, thoughtful insights, and unwavering support. Your companionship has been a source of motivation and inspiration.

Institutional Support: I sincerely appreciate the Department of Mechanical and Aerospace Engineering at Pulchowk Campus for providing the necessary resources, facilities, and a nurturing academic environment.

This thesis is the result of a collective effort, and I am truly grateful for the support and encouragement I have received. Each of you has played a crucial role in shaping this work, and for that, I extend my deepest appreciation.

TABLE OF CONTENTS

LIST OF FIGURES

LIST OF TABLES

LIST OF SYMBOLS

A	Cross-sectional area
ρ	Density
D_p	Downpull
K	Downpull coefficient
∇	Del/gradient
Z	Elevation
d	Gate thickness
H	Operating head
h	Piezometric head
P	Pressure
Re	Reynold's number
γ	Specific weight of water
V_j^2	Square of velocity in the contracted jet under the gate
k	Turbulent kinetic energy
V	Velocity
B	Width of the gate

LIST OF ABBREVIATIONS

CFD	Computational Fluid Dynamics
FEA	Finite Element Analysis
FEM	Finite Element Method
ISMB	Indian Standard Medium Beam
kW	Kilo Watt
MW	Mega Watt
MPa	Mega Pascal
RANS	Reynolds-Averaged Navier-Stokes
VOF	Volume of Fluid

CHAPTER ONE: INTRODUCTION

1.1 Background

Hydraulic gates are extensively employed in irrigation, water supply, and river navigation systems. These gates are generally classified into three categories based on their operational purposes: service gates, emergency gates, and maintenance gates. Based on the mode of operation and movement, gate can also be classified as Vertical lift gates (Fixed wheel gate), Radial gates (Tainter gates), Slide gates, Tilting gates and Fish belly gates. A gate primarily comprises three main components: the leaf, the embedded parts, and the operating device. The leaf, which serves as a movable barrier to water passage, includes the skin plate and girders. The skin plate is the element directly responsible for obstructing the flow of water. The seals, which ensure water tightness, typically consist of rubber strips attached to the skin plate. Additionally, the gate leaf features support elements like wheels, rollers, bearing plates, and guides such as shoes, wheels, and springs (Erbisti, 2014).

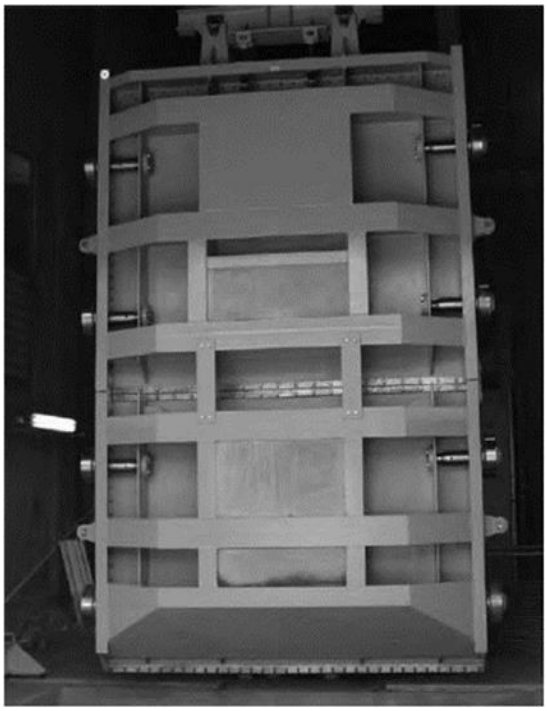

Figure 1.1: Vertical lift fixed wheel gate (Erbisti, 2014)

Vertical lift gates are essential elements in hydraulic engineering, utilized in various structures such as dams, canals, and flood control systems. These gates function by lifting vertically to regulate water flow, playing a vital role in water management and flood prevention (Escobar, 2018).

Embedded parts are structural elements anchored into the concrete framework, serving to guide and support the gate leaf. They help transfer the loads exerted on the gate into the surrounding concrete, safeguard the concrete edges, and provide support for the sealing system. Key components typically include the sill beam, wheel or sliding tracks, side and counter guides, lintel, seal seats, and sometimes a slot lining.

The sill beam forms the bottom horizontal component of the embedded parts, offering foundational support to the gate leaf or bottom seal. In certain gate types—such as sector, drum, and bear-trap gates—it also functions to hold the bottom seal in place. The wheel track bears and spreads the loads transferred by the wheels or rollers, while the slide track serves a similar purpose, accommodating the loads from vertical girders in stoplogs and slide gates. Side and counter guides help prevent lateral movement of the gate leaf and are engineered to withstand the resulting stresses. The lintel, found exclusively in submerged gates, completes the structural waterway frame in conjunction with the sill and side guides. Positioned at the top of the opening, it supports the upper seal and shields the concrete from erosion due to fast-flowing water (Wahab, 2005).

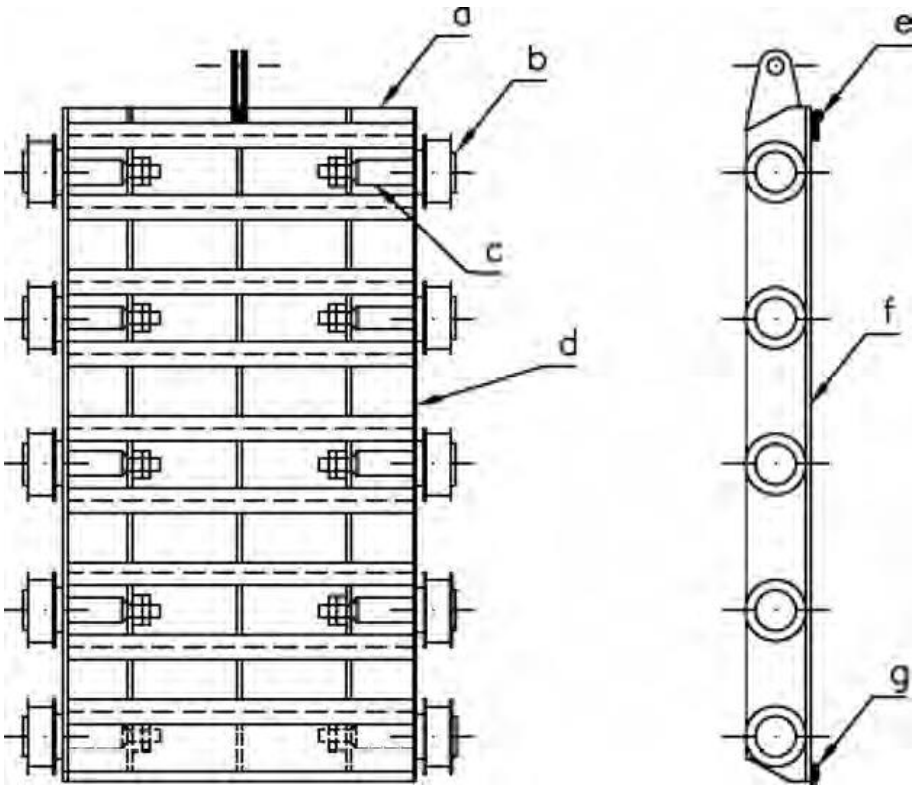

Figure 1.2: Fixed wheel gate nomenclature (Erbisti, 2014)

The labelled parts in the above figure are as: (a) gate leaf; (b) wheel; (c) wheel pin; (d) end girder; (e) top seal; (f) skin plate; (g) bottom seal.

The operating device is responsible for the gate's opening and closing. Some gates, like sector, drum, and bear-trap gates, do not require operating hoists and are instead moved by water pressure (Erbisti, 2014).

1.2 Statement of Problem

Vertical lift gates are essential for regulating water flow in various hydraulic structures, including dams, canals, and flood control systems. Despite their critical role, the complex hydrodynamic forces acting on these gates, particularly when partially open, pose significant challenges to their design and operation.

Key issues include:

- The phenomenon of hydrodynamic downpull caused by high flow velocities and reduced pressures beneath the gate, generates a downward force that can lead to structural failures and operational inefficiencies.
- When a vertical lift gate is partially open, the disturbance in the hydrostatic equilibrium effects in the uneven distribution of the piezometric head. This makes it difficult to predict the exact pressure forces acting on the gate.
- There is need for integration of hydrodynamic analysis into the structural design of vertical lift gates. This gap hampers the development of more resilient and efficient gate designs.

Addressing these problems is vital for improving the safety, reliability, and efficiency of vertical lift gates used in hydraulic engineering applications. This study aims to conduct a detailed hydrodynamic analysis to better understand these forces and their implications for structural design.

1.3 Objectives

Main objective:

- To analyze the hydrodynamic forces in vertical lift gate and evaluate the structural response to these forces using Finite Element Method.

Specific objectives:

- To perform numerical analysis to find the hydrodynamic forces and study flow behavior around vertical lift gate under different operational scenarios.

- To validate numerical results by comparing them with analytical calculations of the force occurred due to the downpull.
- To evaluate the structural response of vertical lift gate to these forces using Finite Element Analysis techniques.

CHAPTER TWO: LITERATURE REVIEW

2.1 Hydrodynamic Force

When submerged in flowing water within the penstock, the gate is subjected to various forces, illustrated in Figure 2.1. The figure depicts the distribution of pressure on each side of the gate. During the gate's closing process, the primary concern is the gate holding force (F_H). The hoist must handle the forces during closing to ensure the gate closes correctly and at the appropriate speed. Once the gate is closed, the holding force should be negative to maintain closure without additional force on top of the gate.

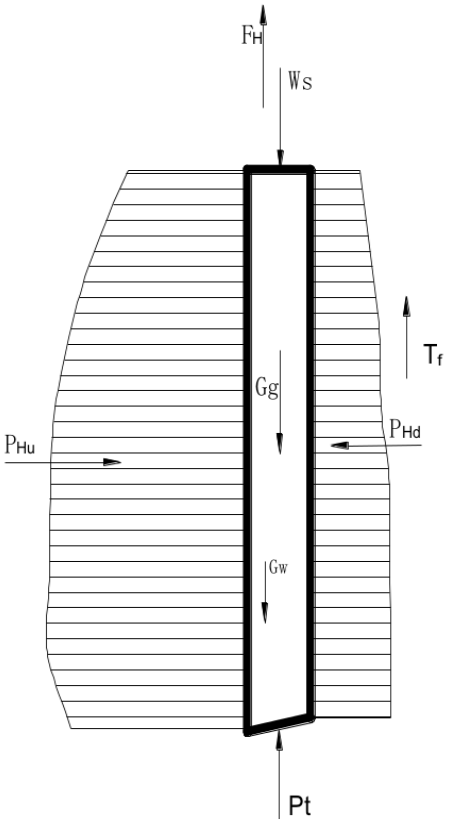

Figure 2.1: Hydrodynamic forces acting on the emergency gate

The gate holding force is expressed as:

$$F_H = G_g + (W_s - P_t) + G_w - T_f \qquad \text{Equation 2.1}$$

where G_g is the weight of the gate, G_w is the weight of water in the gate body (the upstream side of the gate leaf, with the downstream side being mostly hollow), W_s is the water column pressure above the gate, P_t is the uplifting or downpull force on the gate's bottom edge, and T_f is the friction force. The friction force T_f includes the friction from the gate rollers and the water seals, expressed as:

$$T_f = P_H \cdot f \qquad \text{Equation 2.2}$$

Where, $P_H = P_{Hu} - P_{Hd}$

P_H is the horizontal pressure force on the gate, representing the variation between the pressure force acting on the upstream side P_{Hu} and pressure force acting on the downstream side P_{Hd} and f is the comprehensive friction coefficient (MAGNUSSON, 2014).

Calculating hydrodynamic forces on hydraulic gates is a significant challenge in hydro engineering. When flow around the gate becomes unstable, especially when the gate is nearly closed, it leads to variable hydrodynamic loads. These fluctuating forces, induced by different mechanisms, can cause structural vibrations, potentially damaging the structures. The primary mechanisms are:

- Extraneously Induced Excitation (EIE): Pressure fluctuations due to turbulent flow downstream of the gate.
- Instability Induced Excitation (IIE): Vortex shedding leading to flow instabilities.
- Movement Induced Excitation (MIE): Excitation due to fluctuating gate seals.
- Excitation due to (resonating) Fluid Oscillator (EFO): Water surging in a shaft downstream of the gate.

Understanding these flow phenomena as the gate closes is crucial (MAGNUSSON, 2014).

2.2 Flow Phenomena

Both experimental and numerical studies suggest that various flow phenomena can occur around the gate, impacting its functionality and that of the hoist. Analyzing these flow structures is essential to understand their impact and origin. Common flow phenomena observed around gates in hydropower plants include:

- Vortex Shedding
- Streamline Impinging-Leading-Edge-Vortex (SILEV)
- Cavitation

2.2.1 Vortex Shedding

When flow hits the gate leaf, it changes direction and follows the gate wall vertically downward. Upon reaching the leading edge, the flow is deflected away from the gate bottom, creating a separation pocket below the gate. This leads to oscillations in the wake region, causing the flow to roll into vortices that shed from the gate. Alternating vortex shedding, or galloping, can occur with separated flow past an object like an underflow gate.

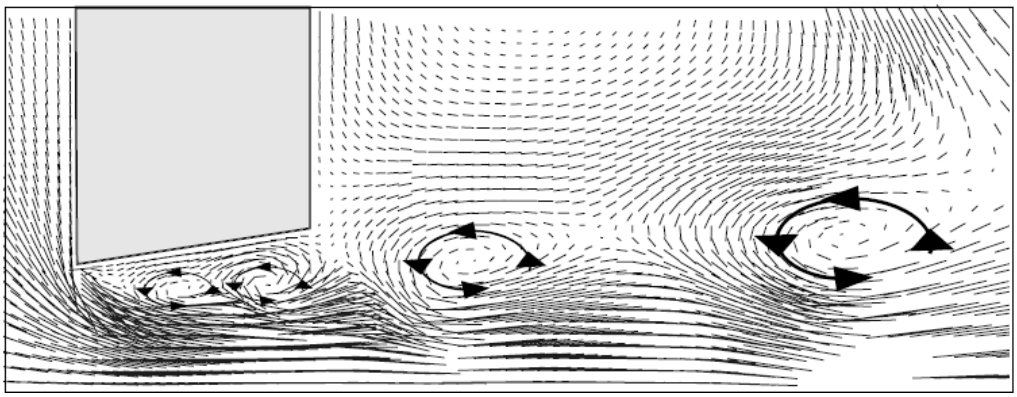

Figure 2.2 Visualization of vortex shedding on a gate (MAGNUSSON, 2014)

2.2.2 Streamline Impinging-Leading-Edge-Vortex (SILEV)

This mechanism involves the detachment of vortices formed below the gate within the separation pocket. Vortices, created by vorticity due to friction, adhere to the boundary, generating torque on the particles. Over time, vortices detach from the bottom wall due to the constant water flow, moving downstream through advection.

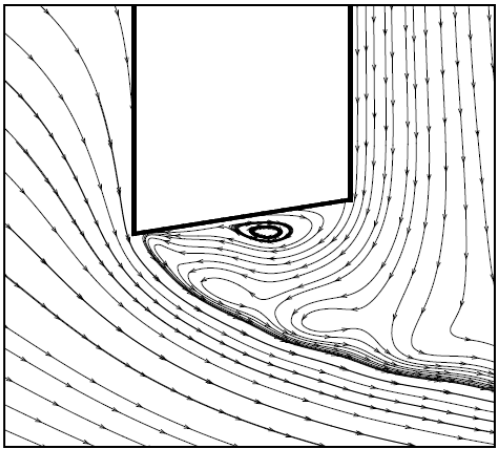

Figure 2.3: Vorticity generated at gate bottom (MAGNUSSON, 2014)

Periodical changes in pressure and flow-induced vibrations occur, forming a recirculation zone downstream of the gate. This movement affects the flow field and pressure distribution at the downstream gate wall, causing pulsating pressure that induces vibrations. These vibrations, regardless of their source, could lead to resonance if their frequency coincides with the gate's natural frequency (MAGNUSSON, 2014).

2.2.3 Cavitation

Cavitation is a flow phenomenon that occurs when the local static pressure in water drops below the vapour pressure, similar to the boiling process. When water is heated, its static pressure increases, and once it reaches atmospheric pressure, air bubbles begin to form. Conversely, cavitation can also occur if the water pressure decreases significantly, falling below a critical threshold far below atmospheric pressure. The primary danger of cavitation lies in the bursting of bubbles when the pressure normalizes, which generates shock waves that exert significant forces on the impacted surface. These forces can cause erosion, damaging the surface. In the context of gate closing processes, cavitation is highly probable due to a high-water head and inadequate aeration. The highly turbulent flow in the separation pocket leads to vortices that drastically reduce the pressure, posing a significant risk of cavitation development (MAGNUSSON, 2014).

2.3 Downpull

Vertical lift gates are particularly favored for emergency gates in conduits due to their easy installation and greater flexibility compared to other gate types. As indicated by their name, vertical lift gates move vertically, controlled by a hoist mechanism. When lifting the gate, factors such as the gate's self-weight, wheel friction, resistance force from friction, and hydrodynamic forces are taken into account.

These gates are typically designed to close under their own weight. One of the major operational concerns with vertical lift gates is the potential underestimation of hydrodynamic downpull forces. These forces are generated due to the formation of a low-pressure zone beneath the gate leaf, which results from the high-velocity water flow. Various geometric features of the gate significantly affect the magnitude of this downpull. Key influencing factors include the length of the gate lip extension, the curvature radius at rounded edges, and the inclination angle of the gate lip. Each of

these elements plays a role in shaping the flow behavior and, consequently, the resulting downward force acting on the gate.

Water is stationary when the gate is completely closed position during which the pressures follow hydrostatic laws, allowing the calculation of hydraulic forces using analytical process. When the water flow is absent, the hydraulic force (vertical) acting on the gate is governed entirely by buoyancy. Under this static condition, the piezometric head remains uniform and stable. However, when the gate is partially opened, this balance is disturbed, resulting in an uneven distribution of piezometric head in the vicinity of the gate. This imbalance arises from the high-velocity flow beneath the bottom surface of the gate, which causes a drop in local pressure due to increased flow speed.

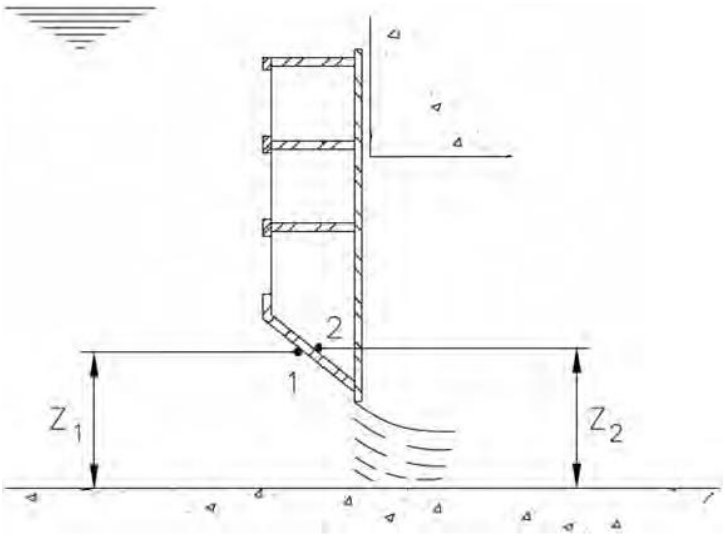

Figure 2.4: Vertical lift gate partially open (Erbisti, 2014)

The vertical lift gate shown in Figure 2.4 is partially open. With reference to the Bernoulli equation to points 1 & 2, we obtain:

$$\frac{P_1}{\gamma} + Z_1 + \frac{V_1^2}{2g} = \frac{P_2}{\gamma} + Z_2 + \frac{V_2^2}{2g} \qquad \text{Equation 2.3}$$

Assuming the water is stationary at point 2, $V_2 = 0$.

Since, Z_1 is almost equal to Z_2, the above equation results,

$$\gamma \frac{V_1^2}{2g} = P_2 - P_1 \qquad \text{Equation 2.4}$$

Since the left hand side of the Equation 2.4 yields a positive value, it indicates differential pressure between points 1 and 2, which becomes more pronounced as the water velocity beneath the gate increases. In point 2, the pressure remains close to the hydrostatic value. This pressure imbalance across the gate's bottom surface creates a net vertical force directed downward, commonly referred to as the downpull. Whereas, the forces arose due to hydrodynamic action are absent in vertical lift gates that have skin plate at upstream side (Erbisti, 2014).

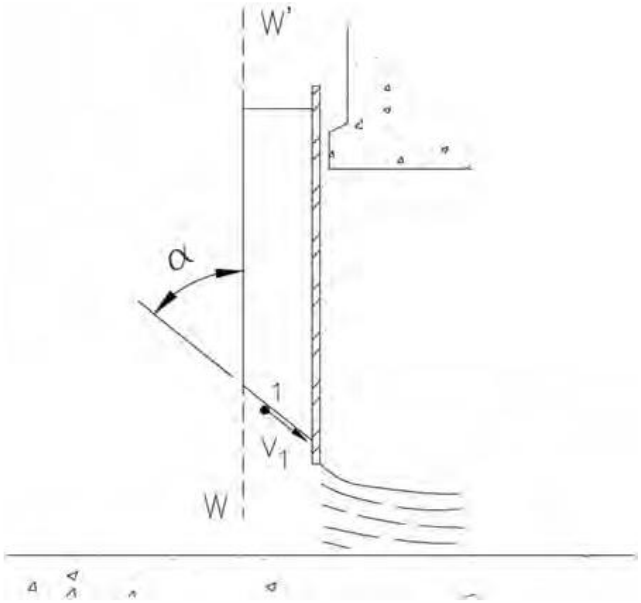

Figure 2.5: Vertical lift gate with downstream skin plate (Erbisti, 2014)

2.4 Factors influencing downpull

Findings from numerous hydraulic model experiments have shown that the magnitude of downpull is significantly influenced by the upstream total head and the cross-sectional area of the gate. This force changes with the gate's degree of opening and is affected by a variety of design and operational factors, including:

- The shape and geometry of the gate bottom, such as the inclination angle, the curvature radius at the upstream edge, and the length of the lip extending below the bottom horizontal beam.
- The extent of the downstream projection of the top seal assembly.
- The size of the gaps between gate and the shaft walls when the gate is partially raised.
- Overall thickness of gate leaf.

- The presence and configuration of clearance in the wall of the gate shaft at downstream.

Each of these factors alters the flow pattern and pressure distribution beneath and around the gate, directly impacting the resulting downpull force.

2.5 Formula for calculation of the downpull

Eqaution for calculation of the downpull is as follows:

$$D_p = \gamma K A H \qquad \text{Equation 2.5}$$

Where,

γ = specific weight (water), in kN/m^3

K = coefficient of downpull

A = gate leaf's cross-sectional area, in m^2

H = head at the gate's bottom, in m (Erbisti, 2014).

However, Naudascher, Kobus, and Rao presented an analytical approach for calculating downpull forces in Hydrodynamic Analysis for High-Head Leaf Gates (UYSAL, 2014). Their technique relies on gate's geometric parameters and the velocity of the contracted jet beneath it. The authors explain that the primary contributor to downpull is the change between the combined distributions of the piezometric head along the upper and lower surfaces of the gate. This force can be determined by:

$$P_1 = (K_T - K_B) B d \gamma \frac{V_j^2}{2g} \qquad \text{Equation 2.6}$$

where:

K_T, K_B= coefficients of top downpull and bottom downpull

B= gate's width

d= thickness of the gate

γ= specific weight (water)

V_j^2 = Square of flow velocity in the jet's constriction.

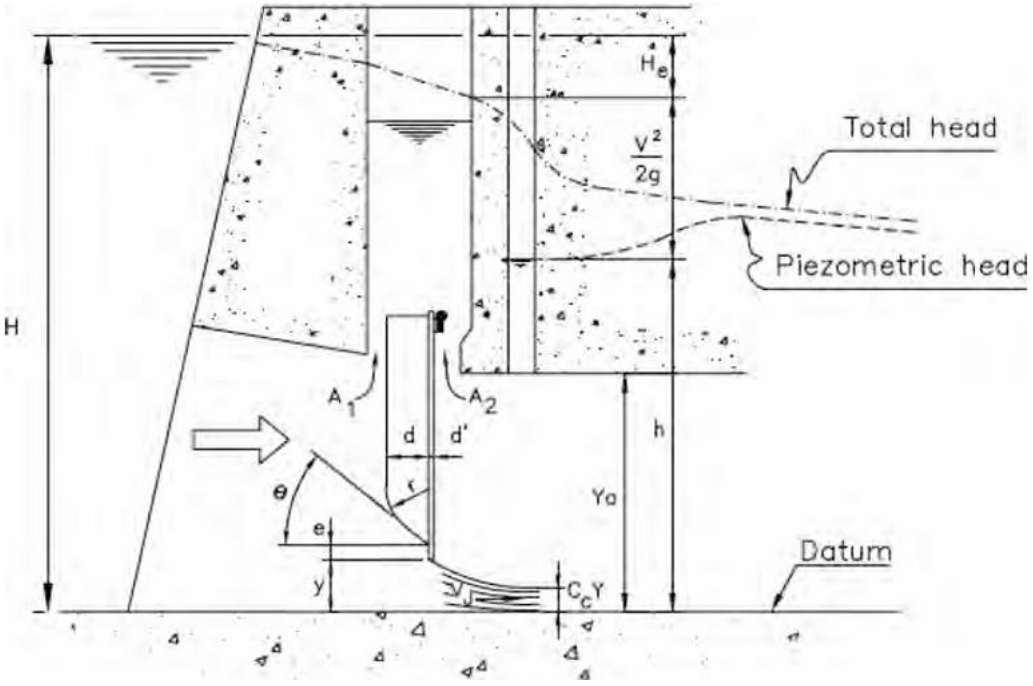

Figure 2.6: Geometric Parameters for Tunnel Gates

Another component of force by downpull arise from the pressure variance acting on the projection at horizontal direction of the gate at top seal. If no water flow is found among the gate and the lintel—meaning the top seal remains compressed beside the wall (downstream)—then A_2 becomes null. In this case, the force on the top seal can be expressed as:

$$P_2 = K_T A_s \gamma \frac{V_j^2}{2g} \qquad \text{Equation 2.7}$$

Another contributing factor to the downpull force comes from the horizontal projection at the top seal, denoted as A_s. If a gap is incorporated into the downstream (vertical wall) of the gate, then A_2 becomes zero, allowing water to flow around the top seal. This flow helps equalize pressure above and below the top seal, effectively eliminating this component of the force by the downpull (Erbisti, 2014).

In the context of gates equipped with an extended skin plate, an additional downpull component arises. This force can be determined using the following equation:

$$P_3 = K_T B d \gamma \frac{V_j^2}{2g} \qquad \text{Equation 2.8}$$

where d represents thickness of the skin plate.

Flow velocity at the vena contracta can be calculated using:

$$V_j = \sqrt{2g(H - H_e - h)}$$ Equation 2.9

where:

H = Total head in the reservoir

H_e = Entrance head-loss

h = Piezometric head at the top of the vena contracta

In the case of free-surface flow, the piezometric head at the flow contraction is determined using the equation:

$$h = C_c y + H_d$$ Equation 2.10

where:

C_c = Coefficient of contraction for the vena contracta

y = Gate opening

H_d = Depression downstream of the gate

Flow velocity at the jet constriction can then be expressed as a function of the gate opening:

$$V_j = \sqrt{2g(H - H_e - C_c y - H_d)}$$ Equation 2.11

The jet velocity reaches its highest value when the gate is just beginning to open (y≈0).

Under submerged flow conditions, it is essential to account for the downstream water head when evaluating the piezometric head at the vena contracta—the point of minimum flow area and maximum velocity underneath the gate. The pressure influenced by both the upstream and downstream water levels, making it a critical factor in assessing downpull forces and overall flow behavior.

When a section exists at the downstream side, the flow dynamics change significantly. As the gate opens, the discharge increases progressively until it reaches the maximum controlled flow rate. Up to this point, the gate opening directly regulates the flow. However, beyond this optimal opening, further increases in the gate height do not result in a proportional increase in discharge. Instead, the velocity of the jet passing beneath the gate becomes the factor of both the gate opening y and the highest achievable flow rate Q, under the assumption that the flow is confined to area beneath the gate leaf.
This velocity can be determined using the equation:

$$V_j = \frac{Q}{C_c A_j} = \frac{Q}{C_c B y}$$ Equation 2.12

where:

A_j = Area of cross-section at the vena contracta

B = gate width

2.5 Governing Equations for Fluid Dynamics

The evaluation of forces caused by downpull on gates is a complex challenge associated with fluid dynamics, encompassing both liquid and gas behavior. Generally, fluid dynamics problems involve solving fundamental partial differential equations governing mass, momentum, and energy conservation.

While analytical solutions exist for simplified cases with specific assumptions, practical engineering applications—particularly those involving turbulent flows and intricate geometries—necessitate numerical solutions. Computational Fluid Dynamics (CFD) provides a framework for analyzing fluid behavior, including flow characteristics, heat and mass transfer, and related phenomena, by applying numerical techniques to solve these governing equations.

Several numerical methods, such as finite difference, finite volume, and finite element approaches, are commonly used for this purpose. For the simulation of vertical lift fixed wheel gates in this study, ANSYS Fluent is employed, which utilizes the finite volume method to compute fluid flow behavior with high accuracy.

- **Continuity equation**: The continuity equation states that rate of mass entering system is equal to the exiting rate from the system along with the addition of mass within the system.

$$\frac{1}{\rho}\frac{D\rho}{Dt} + \nabla \cdot \vec{u} = 0 \qquad \text{Equation 2.13}$$

- **Momentum equation**: The principle of momentum conservation in fluid mechanics is derived by applying Newton's second law to a small fluid element. The total force acting on this element results from three main contributors: gravitational forces, pressure forces, and viscous forces. Since Newton's law states that the net force must equal the mass of the element multiplied by its acceleration, this relationship forms the basis of the momentum equation. If gravity is the only body force considered, it influences the element's motion through its weight. In the case of Newtonian fluids, where shear stress is directly proportional to the rate of deformation, the viscous forces can be expressed in terms of velocity gradients. This

framework leads to the formulation of the momentum conservation law, which is essential for describing fluid motion.

$$\frac{Du_i}{Dt} = \frac{\partial \tau_{ij}}{\partial x_j} + \rho g_i \qquad \text{Equation 2.14}$$

The first term represents the rate of change of momentum per unit volume (or material derivative of velocity). The 2nd term corresponds to surface forces per unit volume, which include stress contributions from viscous and pressure effects. The 3rd term denotes the body forces/unit volume, primarily due to gravitational effects (Escobar, 2018).

2.5.1 Navier-Stokes equation

The equation describes the motion of viscous fluid. The partial differential equation (Equation 2.15) is acquired:

$$\rho \frac{Du_i}{Dt} = -\frac{\partial p}{\partial x_i} + \rho g_i + \mu \nabla^2 u_i \qquad \text{Equation 2.15}$$

Where,

$$\nabla^2 u_i = \frac{\partial^2 u_i}{\partial x_j \, \partial x_j}$$

is known as Laplacian for u_i**.** This equation is valid only in context of incompressible fluids. The equations presented earlier are partial differential equations (non-linear). Due to their complexity, solving these equations analytically is often impractical, making numerical methods on a computer the primary approach. For flow problems of fluid, CFD serves as an effective method for solving these governing nonlinear equations (Escobar, 2018).

2.5.2 Turbulence

Turbulent flow is the most frequently encountered flow type in applied engineering problems. It is highly irregular, unsteady, and three-dimensional in nature. Although turbulence lacks a precise definition, it exhibits several key characteristics. At large Reynold's number, turbulent flow rises. For instance, the shift from laminar flow into turbulent flow generally happens at value greater than 2300. The motion of a turbulent flow is chaotic and irregular. Whereas, it remains predictable and governed by the

Navier-Stoke's equations. Turbulence is caused by the formation of eddies of varying sizes.

Other characteristics are as follows:

- **High Diffusivity**: Due to increased mixing, turbulent flows enhance the transportation of mass, momentum, heat, and chemical species.
- **High Energy Dissipation**: Shear stresses in turbulence result in significant mechanical energy dissipation, leading to greater flow losses and an increase in internal energy, which raises the fluid temperature.
- **Fluctuations**: In a turbulent flow, all physical variables fluctuate over time.

Since turbulent flows are described by the Navier-Stokes equations, numerical simulation methods are used for precise predictions. One such approach is Direct Numerical Simulation (DNS), which resolves the full range of turbulent scales.

A more practical method is Large-Eddy Simulation (LES), where large eddies are computed while small-scale turbulence is modeled. This reduces computational costs compared to DNS, though it still remains resource-intensive for large domains, such as bottom outlets in hydraulic structures.

For most engineering applications, Reynolds-Averaged Navier-Stokes (RANS) models are preferred. These models make computationally efficient while still providing essential engineering quantities like mean velocity, pressure distribution, and wall shear stress. The RANS approach is widely applied in hydraulic engineering due to its balance between computational cost and accuracy (Escobar, 2018).

2.5.3 k-ε turbulence model

It is one of the most widely used turbulence models in engineering simulations based on the Reynolds-Averaged Navier-Stokes (RANS) approach. It is a two-equation linear eddy viscosity model, meaning it introduces two additional transport equations to characterize turbulence properties.

In the context of turbulent kinetic energy k,

Equation 2.16:

$$\frac{\partial(\rho k)}{\partial t} + \frac{\partial}{\partial x_i}(\rho k u_i) = \frac{\partial}{\partial x_j}\left[\left(\mu + \frac{\mu_t}{\sigma_k}\right)\frac{\partial k}{\partial x_j}\right] + P_k + P_b - \rho\epsilon - Y_M + S_k$$

In the case of the turbulent dissipation ϵ, which is responsible for predicting the energy in the turbulent flow.

Equation 2.17:

$$\frac{\partial(\rho\epsilon)}{\partial t}+\frac{\partial}{\partial x_i}(\rho\epsilon u_i)=\frac{\partial}{\partial x_j}\left[\left(\mu+\frac{\mu_t}{\sigma_\epsilon}\right)\frac{\partial\epsilon}{\partial x_j}\right]+C_1^\epsilon\frac{\epsilon}{k}(P_k+C_3^\epsilon P_b)-C_2^\epsilon\rho\frac{\epsilon^2}{k}+S_\epsilon$$

where u_i represents velocity in the given direction, and μ_t is the turbulent viscosity. The term P_k corresponds to turbulence production due to mean velocity gradients, while P_b accounts for buoyancy effects. Y_M denotes fluctuating dilatation effects in compressible turbulence. The terms $S_k$and S_ϵ are user-defined source terms. The constants $C_1^\epsilon,\ C_2^\epsilon,\ C_3^\epsilon, \sigma_k\ and\ \sigma_\epsilon$ are empirical values determined through iterative testing for a wide range of turbulent flows (Escobar, 2018).

2.5.4 Volume of fluid model (VOF)

The VOF model is a modeling (multiphase) approach in ANSYS Fluent for simulating fluid flow involving two or more immiscible fluids, such as air and water. This method is particularly effective when tracking the interface between different phases within a computational domain. The VOF model solves a single set of momentum equations for the entire domain while tracking the volume fraction of each phase throughout the flow field. Given these characteristics, the VOF model is well-suited for simulating the process of a bottom outlet with a vertical lift gate (Escobar, 2018).

Similarly, the model is used to solve a set of momentum equations while the velocity field is communal amongst the phases of the simulation. Different momentum equations used in the VOF model be governed by the volume fractions contained in all phases, which are denoted by the density and viscosity. The general property of the mixture at each computational cell is determined using the volume fraction of every phase.

CHAPTER THREE: METHODOLOGY

3.1 Conceptual Framework

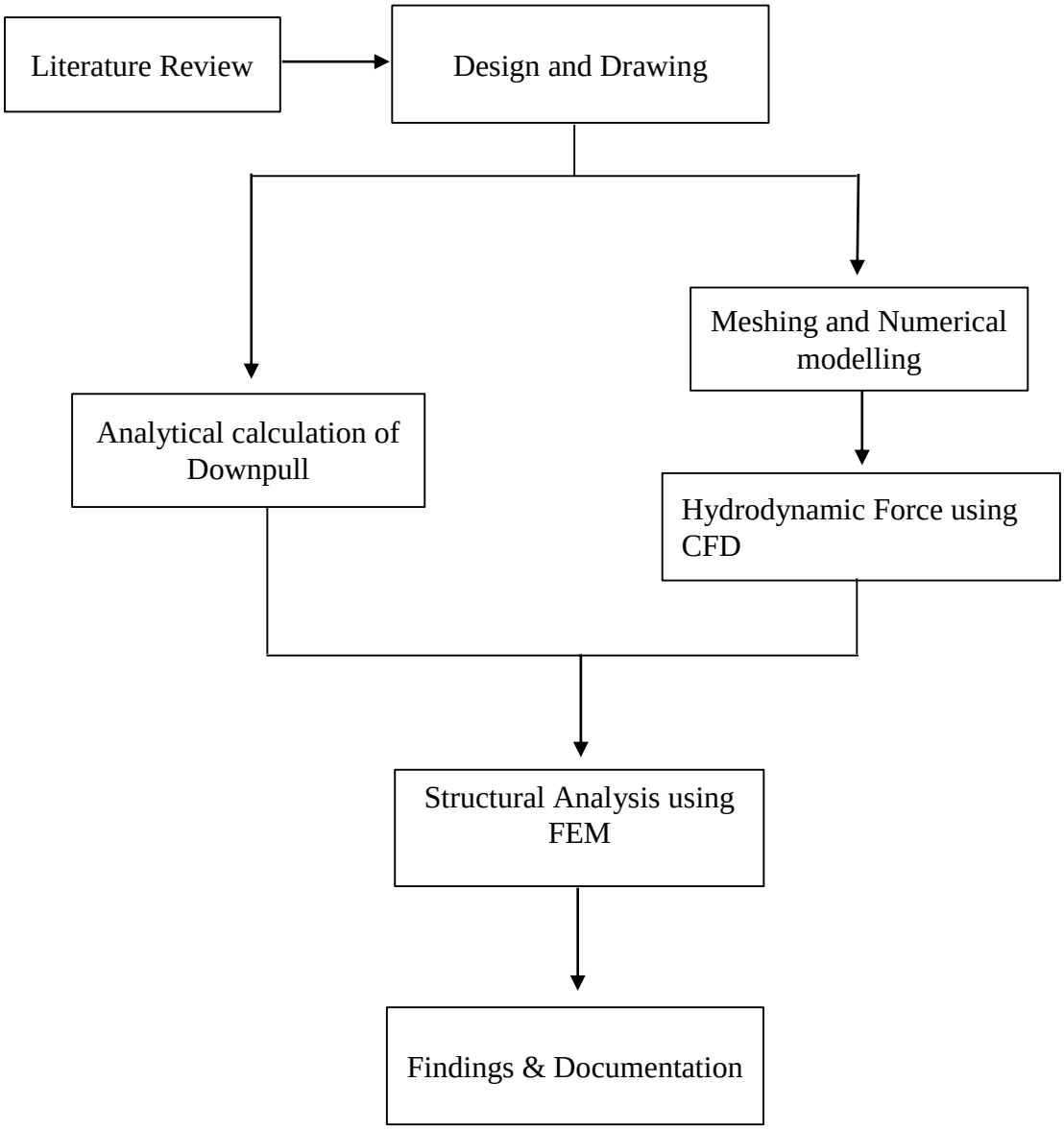

The conceptual framework of the paper outlines the methodology for the research study. It begins with a literature review, which provides a theoretical foundation and understanding of previous works in the field. Based on this review, the design and drawing of 2D and 3D model is created for analysis. This is followed by meshing and numerical modelling, which discretizes the model to prepare them for computational simulations. The study then proceeds with analyzing hydrodynamic force under Different Scenarios Using CFD (Computational Fluid Dynamics) to assess fluid interactions. The results from CFD simulations are used for Structural Response

Assessment, which evaluates the mechanical behavior of the design under different conditions.

3.2 Flow Analysis

The flow analysis simulations were achieved by the ANSYS-FLUENT (version 2019 R3) software. Reynolds averaged Navier-Stokes equations were used in the fluid domain for analyzing hydrodynamic force. Also, the VOF model denoted the two-phase flow contained in the simulation. Numerical result was validated by comparing the simulation result with the analytical methods for downpull calculation. The necessary steps along with the detail for flow analysis of the fluid domain is mentioned below in sequential manner.

3.2.1 Geometry Preparation

Creating a 3-D geometry of the vertical lift gate and its fluid domain was accomplished using Solidworks 2021 software. The design parameters was extracted from gravel flushing gate of the hydro power project named Lower Likhu Hydropower Project (28.1 MW). Table 3.1 presents the characteristics of the gate.

Table 3.1: Gate Parameters

Variable	**Value**
Type of gate	Vertical lift fixed wheel gate
Clear opening width (b)	2000 mm
Clear opening height (h)	1500 mm
Lip angle (θ)	25°
Gate thickness (d)	210 mm

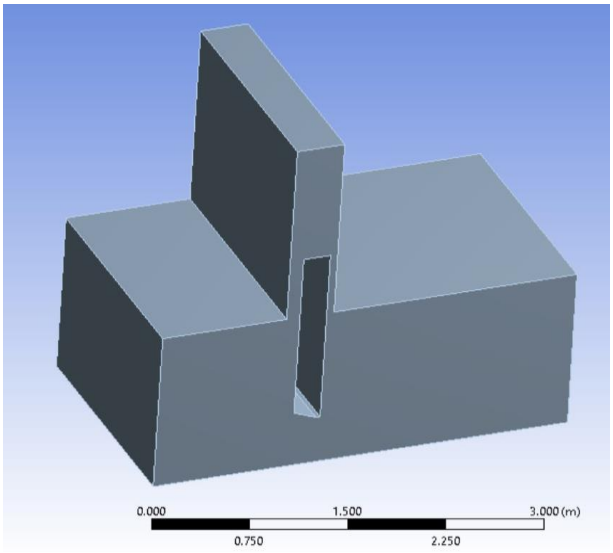

Figure 3.1: Fluid domain of gate setup

3.2.2 Meshing

The meshing setup is optimized for CFD simulation in ANSYS Fluent. The mesh is hybrid, consisting of both structured (quadrilateral) and unstructured (polygonal) elements to accommodate complex flow behavior around the gate. Adaptive sizing of resolution 7 was enabled along with face sizing for element size of 15 mm was added on the boundary of the gate walls to capture boundary layers and downpull forces.

Table 3.2: Mesh Detail Statistics

Parameter	**Value**
Number of Nodes	371063
Number of Elements	347320
Maximum Skewness	0.75

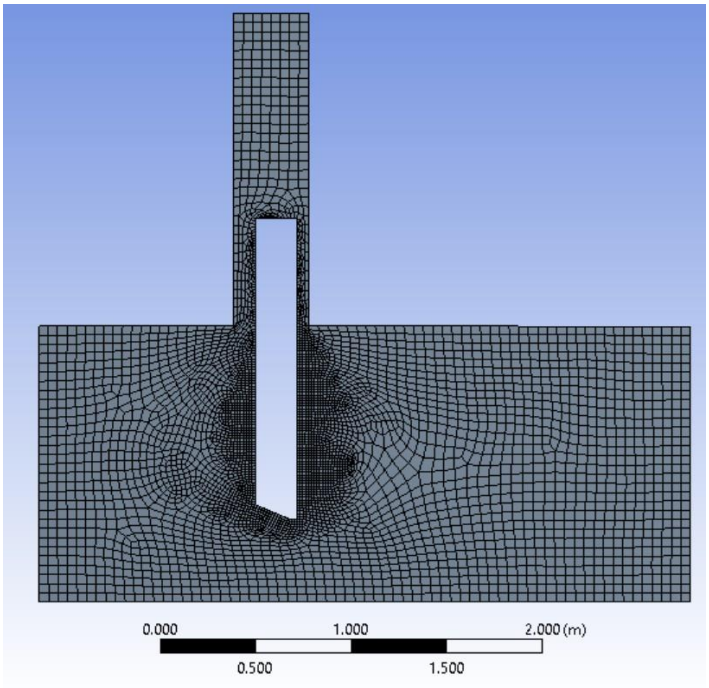

Figure 3.2: Mesh detail of the fluid domain

3.2.3 Models

In the case for simulating the free flow on the surface at the downstream of the gate in the bottom outlet, the Volume of Fluid (VOF) model is selected as the most suitable multiphase modeling approach. This choice is based on the capability of the VOF method to accurately capture the water-air interface.

Table 3.3: Simulation Model Parameters

Constraints	**Value**
Multiphase Model	Volume of Fluid
Turbulence Model	k-epsilon
Turbulence Scheme	Explicit
Phase 1	Water
Phase 2	Air

Although primary objective of the CFD simulations aims to investigate the steady-state behavior of the gate, the VOF scheme (explicit) is applicable to transient simulations only. Thus, an approach for transient case shall be used initially till the flow reaches pseudo-steady state. Since the emphasis is to define the downpull acting on the gate, the "Implicit Body Force" in the VOF model was enabled. The feature enhances

numerical stability and ensures accurate handling of hydrodynamic forces, particularly those acting on the gate surfaces

3.2.4 Boundary Condition

In the simulation, the inlet was set as "mass flow inlet" while the outlet was defined as "pressure outlet" at atmospheric pressure. Wall boundary was set to non-slip condition (velocity set to zero). The mass flow rate of water at inlet was set as 20.94 m3/s while air as zero. The turbulence intensity at the inlet of the culvert and outlets of the model was defined as 5 percent given the turbulent nature of the fluid flow (Escobar, 2018).

3.2.5 Methods and Controls

To predict the governing equations for fluid flow using the chosen models described alongside, numerical methods and solver configurations were employed in spatial discretization, pressure-velocity coupling and transient formulation of the given fluid flow. These settings were selected based on established best practices for the explicit Volume of Fluid (VOF) method. To improve accuracy, second-order discretization was applied to the balance equations. The PISO (Pressure-Implicit with Splitting of Operators) algorithm was used for coupling pressure and velocity, while the PRESTO! method was utilized for pressure interpolation. Gradients were computed using the Least Squares Cell-Based technique. These configurations are commonly employed in computational fluid dynamics (CFD) and did not adversely affect the stability of the solution (Hao Zhe Khor, 2023).

For ensuring convergence, the global Courant number was maintained at 2, with a preliminary time step of 0.001 second. Additionally, an adaptive time-stepping approach, governed by the Courant number, was enabled. Each time step initially included 20 iterations which was sufficient to maintain convergence.

3.3 Structural Analysis

The static structural analysis was done using the commercial solving ANSYS (version 2019 R3) software. The assessment was done by evaluating the maximum principal stress and total deformation of the model (MAGNUSSON, 2014).

3.3.1 Design and Modeling

Creating a 3D geometry of the vertical lift gate and its fluid domain was accomplished using Solidworks 2021 software. The design parameters were extracted from gravel

flushing gate of the hydro power project named Lower Likhu Hydropower Project (28.1 MW). Table 3.4 presents the design parameters of the gate.

Table 3.4: Gate Design Parameters

Variable	**Value**
Type of gate	Vertical lift fixed wheel gate
Design head (H)	10.67 m
Seal Span (B)	2100 mm
Roller span (L)	2200 mm
Hydrostatic load (W)	31.25 Ton
No. of horizontal beams (n)	4
Type of horizontal beam	ISMB 250
Thickness of skin plate	10 mm
Inner vertical Girder	Flat (200 mm x 10 mm)
Side Vertical Girder	ISMC 250
No. of main rollers	4

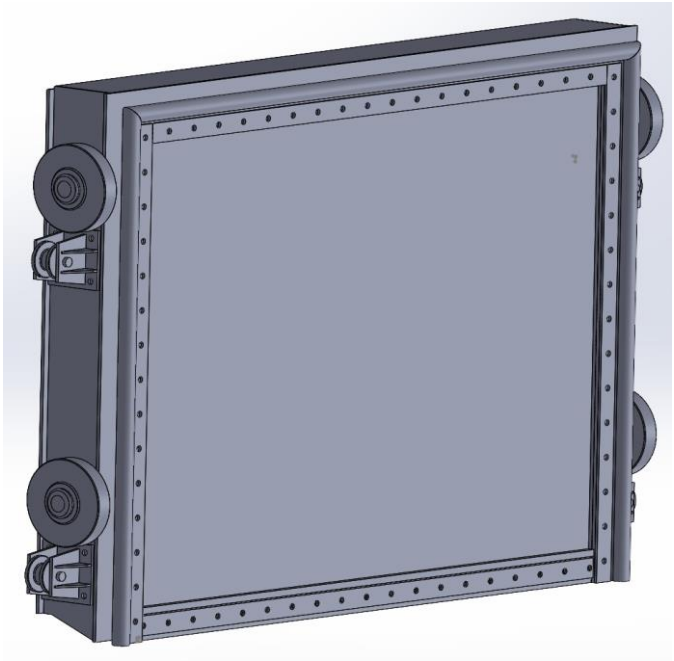

Figure 3.3: 3D Isometric view of Vertical lift gate

All parts of the assembly model were assigned structural steel as material with grade IS 2062: E250. The properties of the material is given below:

Table 3.5: Material Properties of Structural Steel

Variable	**Value**
Density	7850 kg/m³
Young's Modulus	2e+11 Pa
Poisson's Ratio	0.3
Coefficient of thermal expansion	1.2e-5 /◦C
Ultimate Strength	410 MPa
Yield Strength	250 MPa

3.3.2 Meshing

The meshing process was carried out in ANSYS Mechanical, applying a structured meshing approach with a body sizing control to ensure uniform element distribution across the model. The element size was set to 50 mm. The generated mesh primarily consists of hexahedral elements, with tetrahedral elements incorporated in regions of complex geometry. This meshing strategy ensures adequate resolution for analyzing stress distribution and deformation while keeping computational costs manageable.

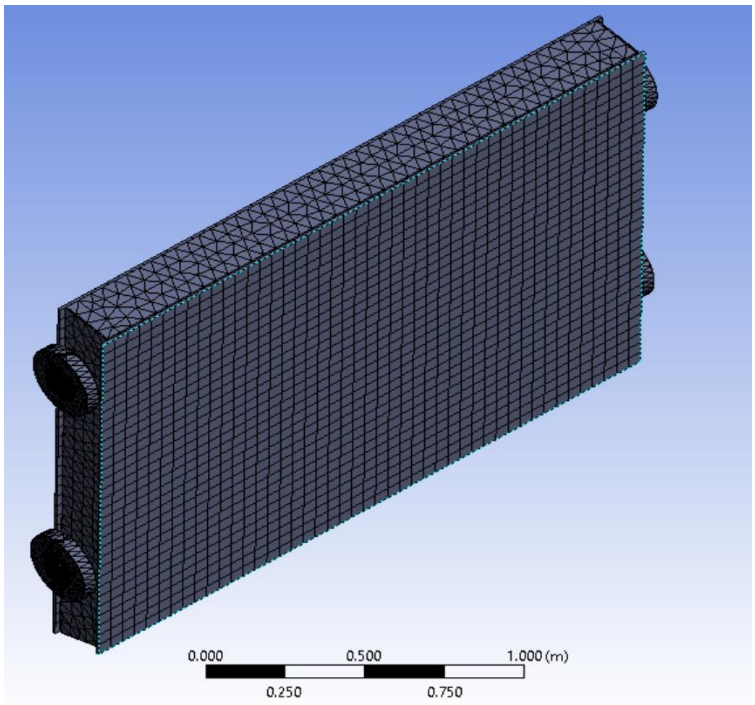

Figure 3.4: Meshing of the 3D CAD model

3.3.3 Loading Conditions

In the structural analysis of the gate, three primary types of loads are considered to evaluate the gate's performance under realistic operational scenarios. The gate structure is supported and constrained by four rollers and fixed at the side edges, restricting its translational movement and simulating actual boundary conditions during operation. A significant hydrostatic load of 31.25 tons is exerted at the upstream side of the gate. This load represents the exerted pressure by the water retained behind the gate and acts uniformly across the submerged surface. The standard earth gravity load is exerted in the downward direction to simulate the self-weight of the gate and its components. An additional downpull force, derived from computational fluid dynamics (CFD) analysis of water flow over and around the gate, is included. This force represents the dynamic interaction between the flowing water and the gate structure, often occurring when the gate is partially or fully opened. It acts downward and can significantly influence the stress distribution and deflection, especially near the seals and supporting structures. These combined loads are applied to evaluate the structural performance of the gate under service conditions. The analysis focuses on determining the maximum principal stress, Von Mises stress, and total deformation within the gate components. These stress metrics help identify potential failure zones, validate the design under critical loading scenarios, and ensure the gate maintains structural safety and functional reliability throughout its operation.

CHAPTER FOUR: RESULTS AND DISCUSSION

4.1 Hydrodynamic Field

The pressure contours for gate openings of 20%, 40%, 50%, and 80% provide insight into the flow characteristics and pressure distribution at different gate positions. As shown in the images below, the pressure distribution changes significantly with the gate opening.

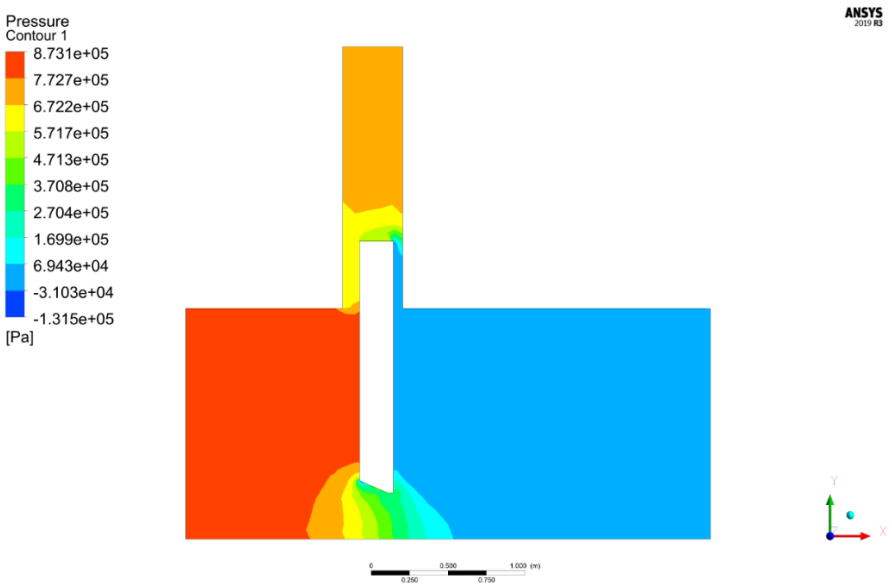

Figure 4.1: Pressure Contour for 20% Opening

At 20% gate opening, a significant pressure drop occurs across the gate, leading to a more pronounced low-pressure region downstream compared to larger openings. The upstream side experiences high pressure, as indicated by the red region, while the downstream side shows a strong low-pressure zone (blue region), suggesting high-velocity flow through the narrow passage. This configuration can cause flow turbulence, cavitation, and potential energy losses

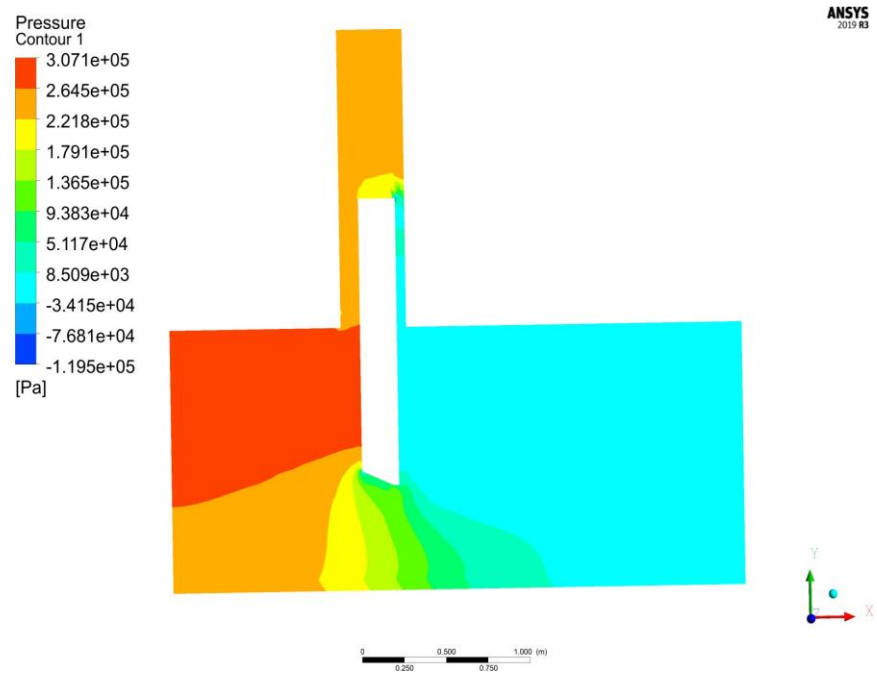

Figure 4.2: Pressure Contour for 40% Opening

At 40% gate opening, the pressure near the gate lip is relatively high, with a localized low-pressure region downstream. The presence of a pressure gradient indicates a rapid acceleration of the flow, leading to a substantial drop in pressure. This low-pressure region could contribute to cavitation risks and increased downpull forces acting on the gate.

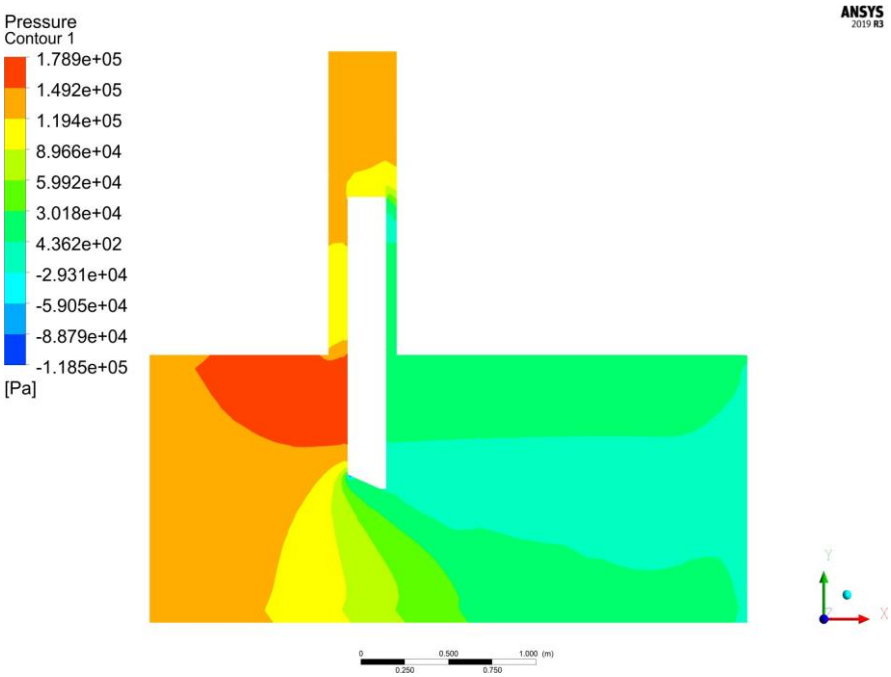

Figure 4.3: Pressure Contour for 50% Opening

At 50% gate opening, the pressure distribution becomes more balanced, with a gradual transition in the contours. The low-pressure region downstream is still present but reduced compared to the 40% opening. This indicates that as the gate opening increases, the pressure distribution at downstream becomes more uniform, reducing the likelihood of adverse effects like cavitation and downpull.

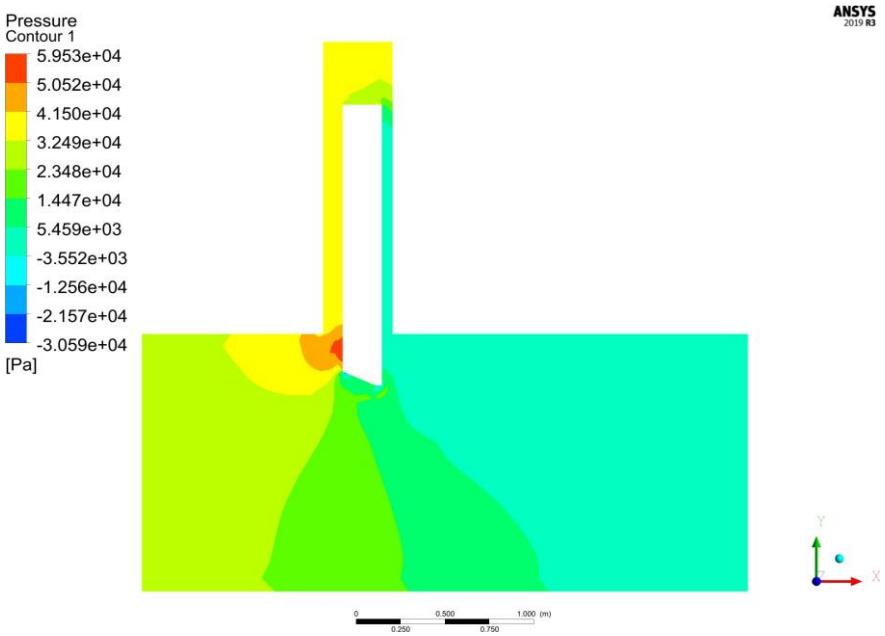

Figure 4.4: Pressure Contour for 80% Opening

At 80% gate opening, the flow becomes more stabilized, and the pressure contours show a more even distribution. The low-pressure region downstream is minimized, and the high-pressure region at the gate bonnet remains relatively constant. This suggests that for larger gate openings, the pressure forces acting on the gate become more predictable, improving operational stability.

These findings highlight the importance of considering pressure distribution when designing and operating gates, ensuring optimal performance while minimizing undesirable effects such as downpull and cavitation.

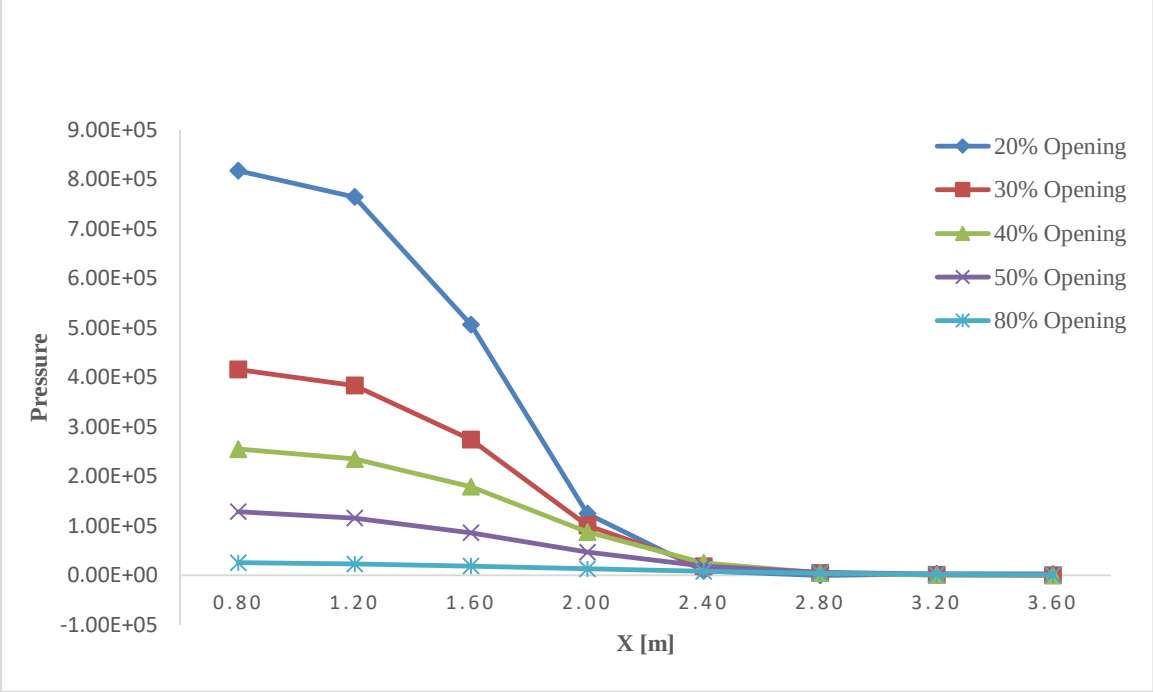

Figure 4.5: Pressure change curve for different gate openings

Figure 4.5 presents the pressure variation curves at y= 0.1 m in the XY plane, depicting the pressure distribution for five different gate openings. The gate is positioned at a distance of x= 1.75 m. As observed, the highest pressure values are concentrated on the upstream section, while the lowest pressure values occur immediately downstream of the gate. This trend is consistent across all five gate openings.

A notable characteristic of the pressure distribution is its dependence on the gate opening size. When the gate opening is small, a significant pressure difference is observed between the upstream and downstream regions. This sharp pressure gradient results from the restricted flow passage, which leads to increased resistance and a buildup of pressure on the upstream side, followed by a rapid drop on the downstream side. Conversely, as the gate opening increases, the pressure difference diminishes, allowing for a smoother and more uniform distribution of pressure across the flow domain.

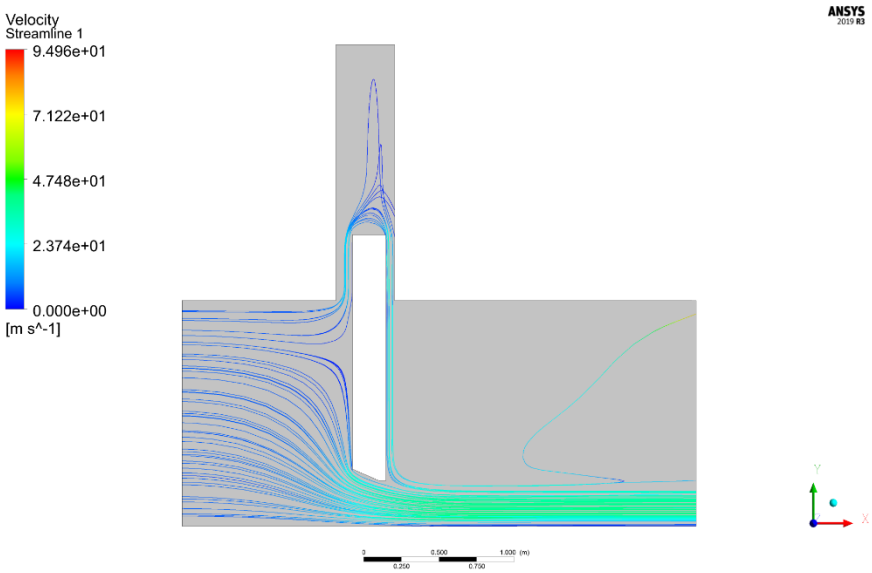

Figure 4.6: Velocity Streamlines at 20% opening

Figure 4.6 illustrates the velocity streamlines of fluid flow through a partially opened gate at 20% opening. At this narrow opening, the flow accelerates significantly as it passes through the gate, creating a high-velocity jet downstream. The streamlines show smooth, uniform flow upstream, while downstream, the flow remains a free surface flow i.e. velocity is changing minimally despite gate position. Additionally, recirculation zones and eddies are visible near the gate edges, indicating flow separation and turbulence due to the restriction.

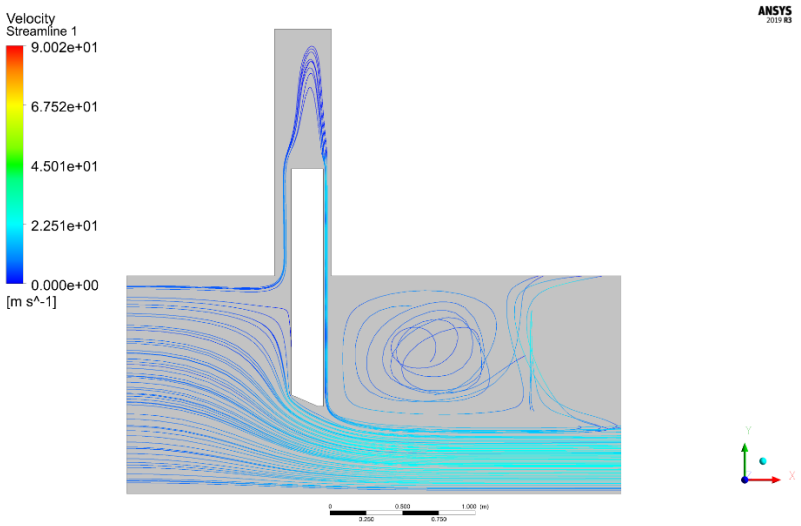

Figure 4.7: Velocity Streamlines at 40% opening

Figure 4.7 visualizes the fluid flow through a gate opened to 40%, using ANSYS CFD simulation. Compared to the 20% opening, the wider opening allows more water to pass

through, reducing the velocity of the jet downstream. However, recirculation zones are more distinct, especially downstream, where a large vortex forms due to flow separation. This eddy region indicates areas of low-energy swirling flow, which can contribute to energy dissipation and turbulence.

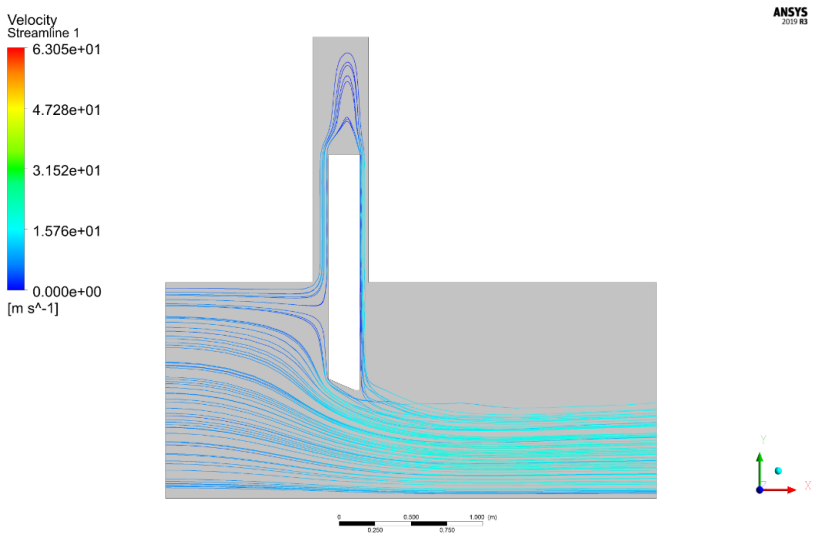

Figure 4.8: Velocity Streamlines at 50% opening

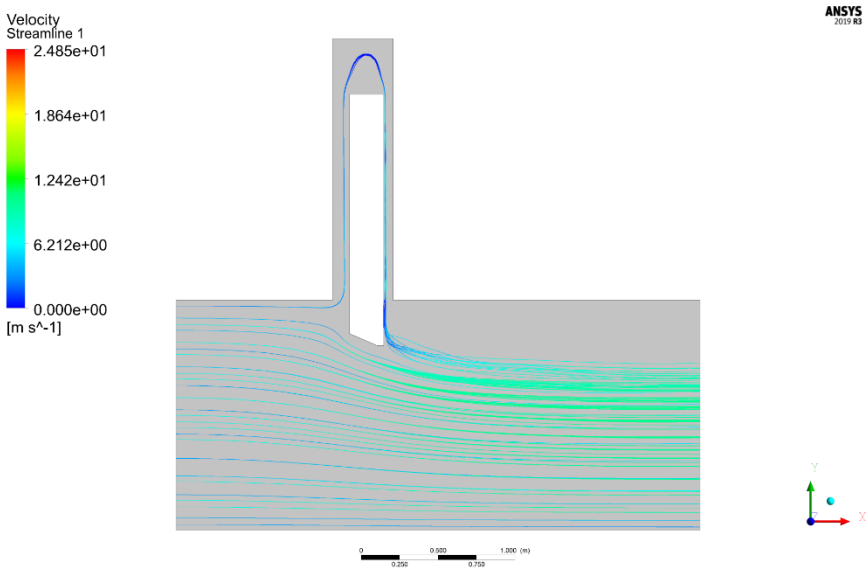

Figure 4.9: Velocity Streamlines at 80% opening

In Figure 4.8 (50% gate opening) and Figure 4.9 (80% gate opening), the flow accelerates through the partially opened gate, generating a high-velocity jet downstream. The wider opening allows for a smoother and more uniform flow, with less turbulence and negligible recirculation zones. The velocity distribution is more balanced, reducing flow disturbances and minimizing energy losses.

As the gate opening increases, the flow becomes more stable, reducing the potential for cavitation and structural wear.

4.2 Downpull

Table 4.1 presents the downpull exerted on the gate for various gate openings in the culvert, as calculated from CFD simulations of the 25° lip gate. The downpull force is determined by subtracting the force of bottom downpull from the top downpull, yielding the net hydrodynamic force at vertical direction acting on the gate.

Table 4.1: Downpull Force for Different Gate Openings.

Gate Opening	**Numerical (kN)**
10%	22.32
20%	42.52
30%	48.41
40%	47.90
50%	42.84
60%	38.52
80%	14.43

As the gate opens, the pressure difference between the upstream and downstream sides, along with flow acceleration, influences the magnitude of the downpull. Initially, as the gate opens from a fully closed position, the downpull force increases due to rising velocity and suction effects. It reaches a peak at around 30% opening, where the combined effect of flow-induced pressure and hydrodynamic forces is maximized. Beyond this point, the downpull force gradually decreases as the gate opens further, reducing pressure differentials and stabilizing the flow.

4.3 Validation of Numerical Results

In this study, the numerical results derived from the CFD model were validated against the analytical approach presented in Design of Hydraulic Gates by Paulo C.F. Erbisti, specifically in Chapter 8, Example 8.1 (Erbisti, 2014).

For the analytical calculation of downpull, the total downpull acting on the gate was determined by summing three forces.

$$P_1 = (K_T - K_B) B d \gamma \frac{V_j^2}{2g}$$ Equation 4.1

P_1 is the downpull force due to the pressure difference between the top and bottom surfaces of the gate. Also, K_T & K_B are top and bottom downpull coefficients respectively. B, d and V_j are gate width, gate thickness and velocity in the vena contracta respectively.

$$P_2 = K_T A_s \gamma \frac{V_j^2}{2g}$$ Equation 4.2

P_2 is the downpull force due to the pressure difference acting on the extended skin plate. *As* is the area of horizontal projection of the top seal

$$P_3 = K_T B d \gamma \frac{V_j^2}{2g}$$ Equation 4.3

P_3 is the downpull force due to the lintel seal protrusion at the top of the gate.

The analytical method provides a theoretical estimation of the downpull acting on the gate centered on hydraulic principles, while the CFD simulation captures the complex flow behavior numerically. The comparison between these two approaches is presented in the Table 4.2 and graph (Figure 4.10) below, showing a good correlation between the numerical and analytical results.

Table 4.2: Comparison of Downpull Force

Gate Opening	**Downpull Force (kN)**	
	CFD	**Analytical**
10%	22.32	16.95
20%	42.52	35.46
30%	48.41	44.09
40%	47.90	44.83
50%	42.84	41.11
60%	38.52	34.41
80%	14.43	12.04

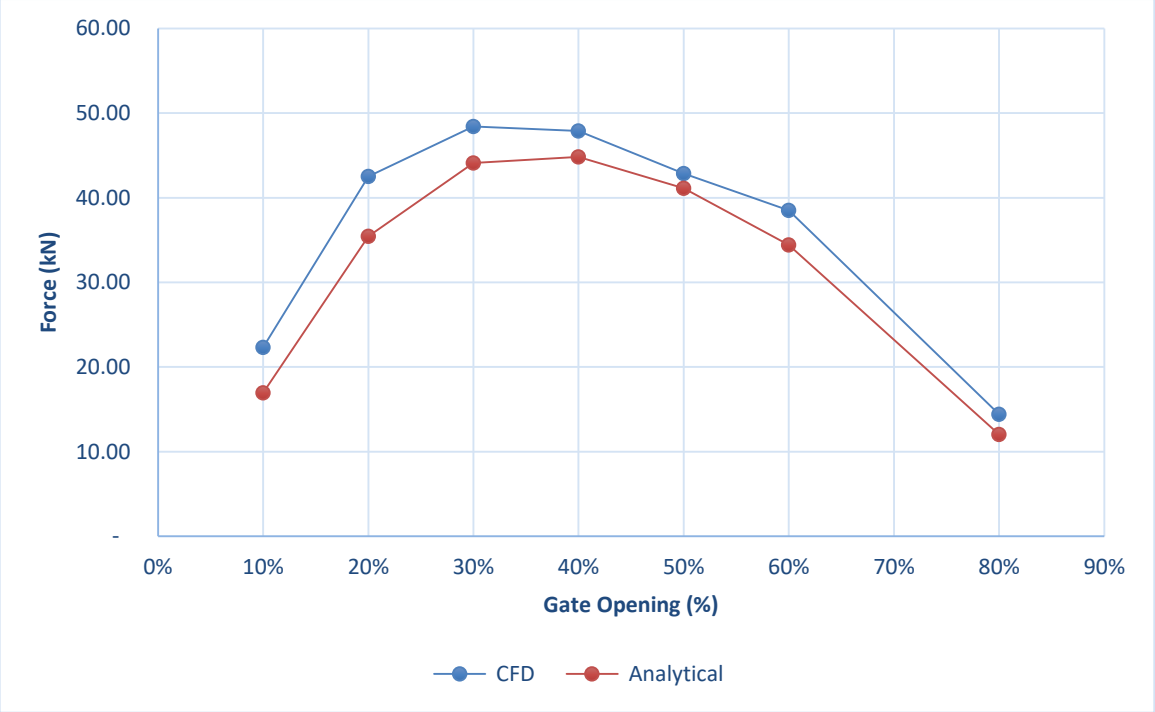

Figure 4.10: Downpull Force-CFD vs Analytical

The peak downpull force occurs around 30% gate opening, with numerical results slightly exceeding analytical values, likely due to additional effects such as flow separation and pressure variations. Beyond this point, the force decreases as water flow stabilizes. Minor deviations between the methods, particularly at 30%-50% openings, may arise from numerical approximations or turbulence modeling.

4.4 Finite Element Analysis

The computed downpull forces from the numerical (CFD-based) were applied for the structural analysis of the gate using the Finite Element Method (FEM). This analysis aimed to assess the maximum principal stress, equivalent stress and total deformation under the given loading conditions. The comparative images (Figure 4.11 and Figure 4.12) illustrate the maximum principal stress on the gate with and without downpull, while maintaining all other constraints unchanged.

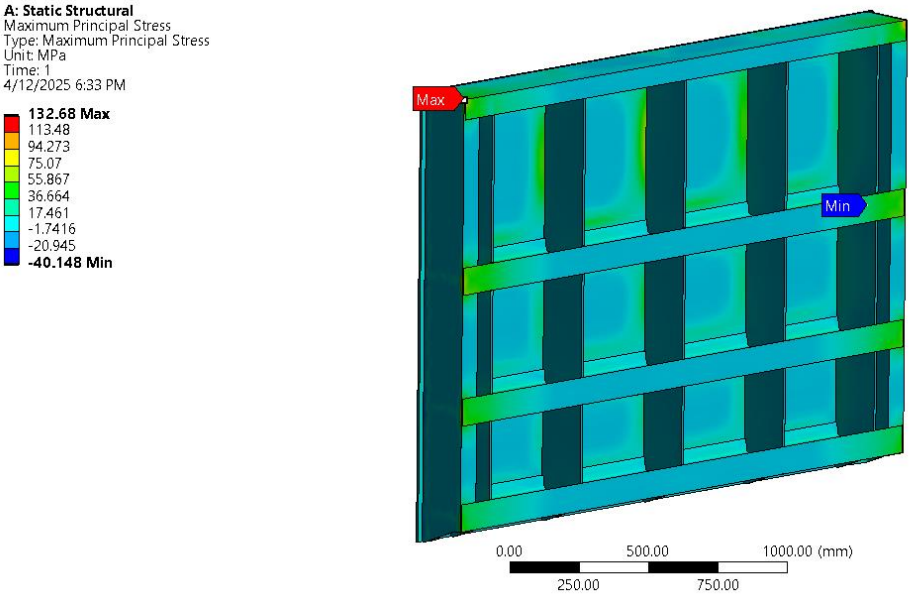

Figure 4.11: Maximum Principal Stress without Downpull

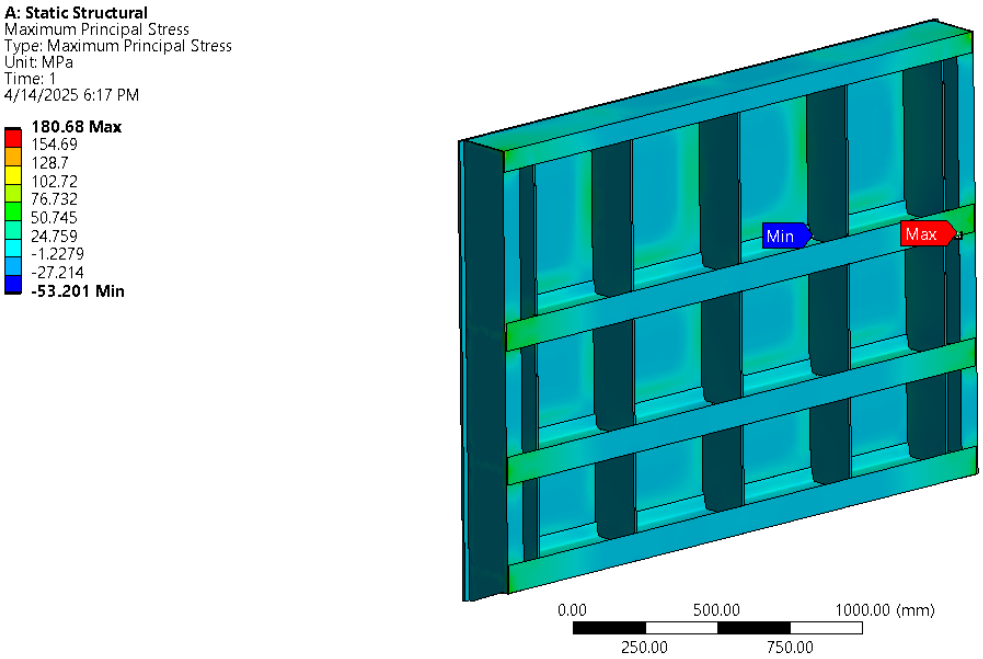

Figure 4.12: Maximum Principal Stress with Downpull

The finite element analysis (FEA) results for maximum principal stress under different loading conditions reveal significant variations in stress magnitudes and distributions. In the first case i.e. Figure 4.11, the maximum principal stress is observed to be 132.68 MPa, while in the second case i.e. Figure 4.12, it increases significantly to 180.68 MPa.

This suggests that the second loading condition exerts greater forces on the gate structure due to increased downpull forces or additional boundary constraints. In both analyses, the maximum stress concentrations are observed at the top corners of the gate, as indicated by the red regions. The high stress appeared at the corner is likely due to geometry edge and doesn't reflect actual part failure risk. However, the stress in the Figure 4.12 are slightly higher than the stresses observed at the Figure 4.11 which highlights the need of integrating downpull forces in the design of the gate.

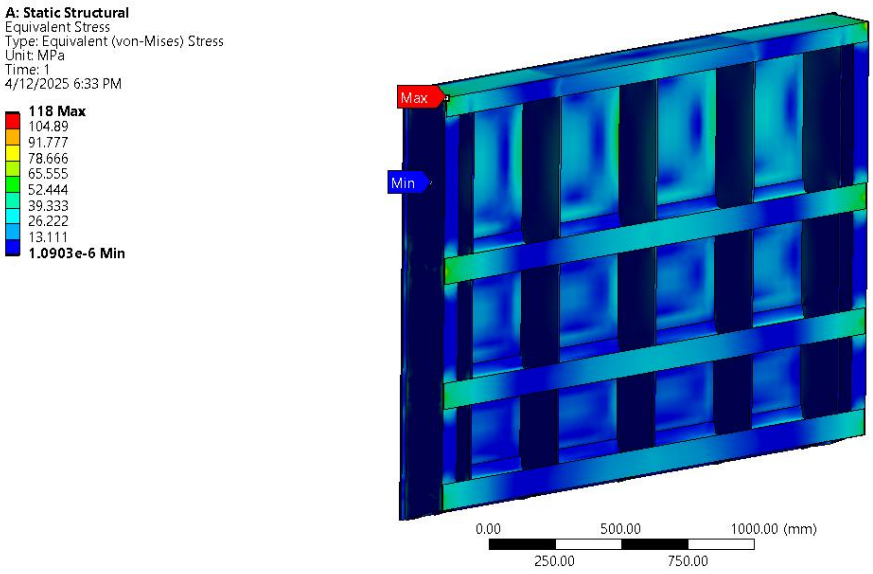

Figure 4.13: Equivalent Stress without Downpull

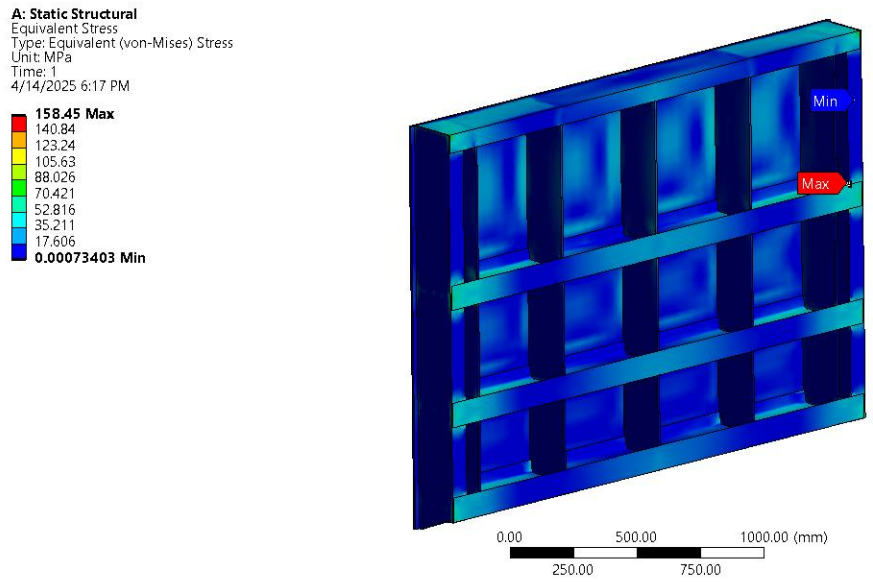

Figure 4.14: Equivalent stress with Downpull

The finite element analysis (FEA) results in Figure 4.13 and Figure 4.14 reveal a significant increase in equivalent (von Mises) stress when downpull forces are applied. Without downpull, the maximum stress is 118 MPa appearing in localized areas whereas with downpull, it rises to 150.45 MPa, marking an increase of approximately 27.5 %. This indicates that downpull exerts substantial additional forces on the structure, affecting its overall stress distribution. In both cases, peak stresses appear in similar regions observed at the corners/edges likely due to geometry edge and doesn't reflect actual part failure risk. Similarly, the analytical calculation of the equivalent stress at the beams are calculated for both case and compared with the numerical result.

Table 4.3: Comparison of Equivalent Stress (Without Downpull)

Beam no.	**Beam Selection**	**Equivalent stress (N/mm^2)**	
		Analytical	**Numerical**
Main Horizontal Beam			
1	ISMB 250	41.19	61.38
2	ISMB 250	69.32	72.05
3	ISMB 250	55.1	54.86
4	ISMB 250	56.22	54.79
End Vertical Girder			
5	ISMC 250	79.95	84.77

Table 4.4: Comparison of Equivalent Stress (With Downpull)

Beam no.	**Beam Selection**	**Equivalent stress (N/mm^2)**	
		Analytical	**Numerical**
Main Horizontal Beam			
1	ISMB 250	42.11	65.58
2	ISMB 250	69.87	73.97
3	ISMB 250	55.80	57.48
4	ISMB 250	56.90	60.32
End Vertical Girder			
5	ISMC 250	83.23	87.09

The End Vertical Girder (Beam 5, ISMC 250) withstands significantly more load compared to the Main Horizontal Beams (Beams 1-4, ISMB 250), as evident from the above Table 4.3 and Table 4.4. The end vertical girder shows an analytical stress of 83.23 N/mm² and a numerical stress of 87.09 N/mm², which are notably higher than the maximum stresses observed in the horizontal beams (Beam 2: 69.87 N/mm²

analytical, 73.97 N/mm² numerical). This difference arises because the vertical girder acts as a primary load-bearing member, resisting reaction forces from multiple horizontal beams, along with additional lateral and torsional stresses from external loads like water pressure or wind. Furthermore, the ISMC 250 (channel section) has lower bending stiffness compared to the ISMB 250 (I-beam), making it more susceptible to higher stresses under similar loading conditions. The numerical (FEA) stresses being greater than analytical values also indicate localized stress concentrations in the vertical girder, likely at connections or support points. Given these factors, the vertical girder is the most critical component in the gate structure.

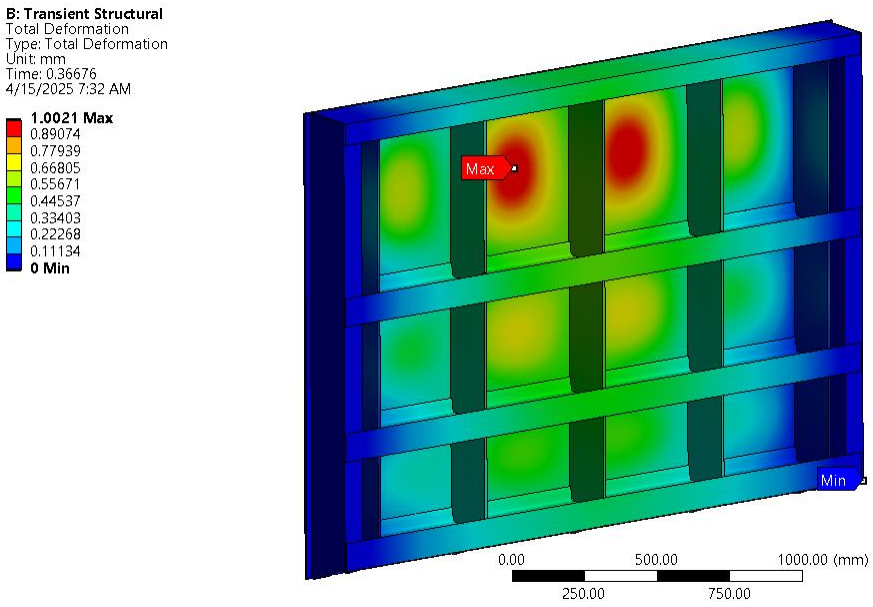

Figure 4.15: Total Deformation without Downpull

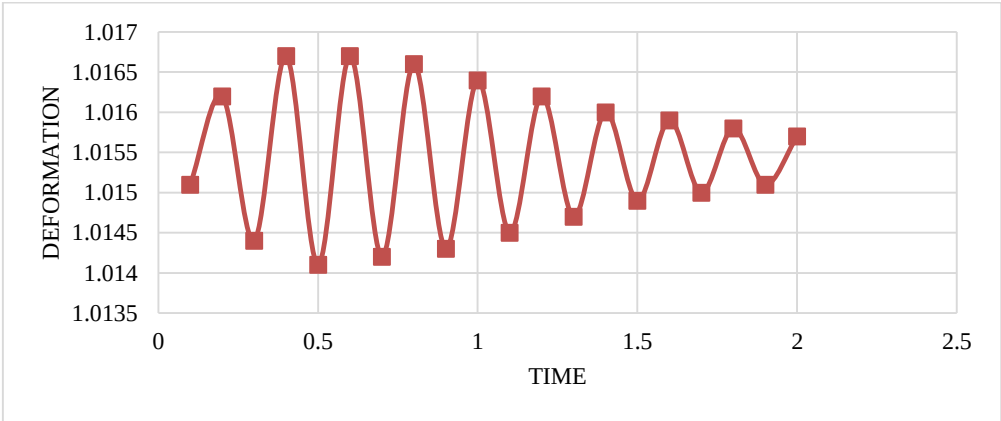

Figure 4.16: Graph of Deformation VS Time (Without Downpull)

Figure 4.16 presents a plot of total deformation vs. time. This graph captures the system's dynamic response over a span of 2 seconds. The deformation exhibits an

oscillatory pattern, characteristic of a damped dynamic system. The amplitude of oscillations gradually decreases, indicating energy dissipation. The presence of high-frequency oscillations reflects the transient nature of loading conditions, possibly caused by sudden external forces or fluid-structure interaction scenarios.

Overall, these results validate the structural integrity of the gate under dynamic loading while also highlighting critical regions of stress concentration that may require design attention for fatigue or long-term durability if it exceeds the allowable deformation limiting value.

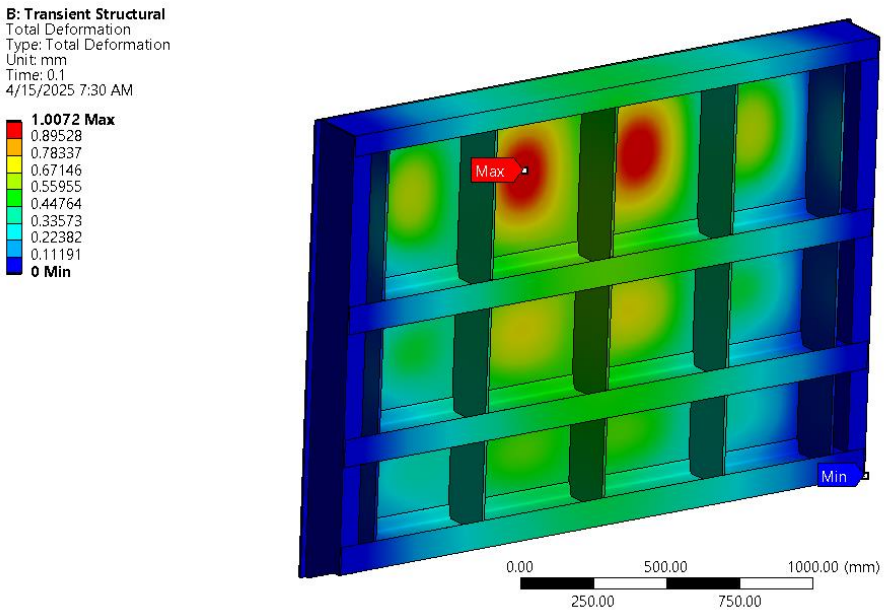

Figure 4.17: Total Deformation with Downpull

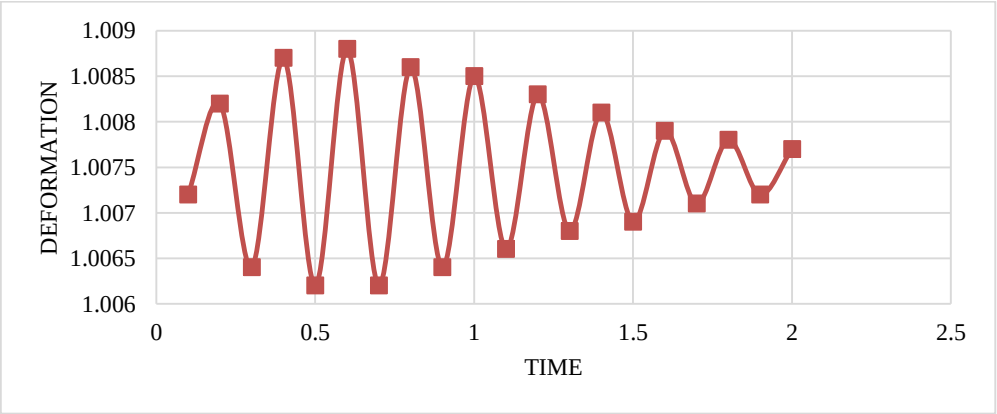

Figure 4.18: Graph of Deformation VS Time (With Downpull)

Figure 4.18 presents the time-history plot of total deformation of the gate structure when subjected to downpull forces, as part of a transient dynamic analysis. This graph complements the structural deformation contour previously shown in Figure 4.17 and provides a temporal insight into how the deformation evolves over a 2-second interval.

The curve demonstrates a damped oscillatory response, characteristic of dynamic systems subjected to impulse or transient loads. The maximum deformation oscillates around 1.0085 mm, consistent with the static maximum value of 1.0072 mm observed in the FEA contour plot. This alignment validates the simulation and reflects realistic system behavior. The initial oscillations show larger amplitudes, which gradually decay over time, indicating the presence of damping in the system. This damping could be attributed to material properties, joint friction, or interaction with the surrounding fluid environment. The deformation does not stabilize to a constant value, which confirms the dynamic nature of the load and the structure's continuous response. Such results are crucial for assessing long-term performance and fatigue behavior, especially in gates exposed to fluctuating hydraulic conditions.

CHAPTER FIVE: CONCLUSIONS AND RECOMMENDATIONS

5.1 Conclusion

This study investigates the hydrodynamic forces acting on a vertical lift gate, focusing on pressure distribution, downpull forces, and their impact on structural integrity. The downpull forces peak at around 30% gate opening, as observed in both CFD and analytical calculations. The force increases rapidly from 10% to 30% opening, reaching a peak of approximately 48.41 kN (CFD) and 44.09 kN (Analytical). Beyond 30% opening, the force remains nearly constant up to 40% opening, after which it gradually decreases. At 80% opening, the force drops significantly to around 10–15 kN, indicating reduced flow-induced loading. The validation of CFD results against analytical calculations showed strong agreement, providing assurance in numerical simulations for predicting hydrodynamic behavior.

The structural analysis determines that accounting for downpull forces in the gate design results in an evident increases in both stress and deformation parameters. The maximum principal stress exhibited an increase from 132.68 MPa to 180.68 MPa, while equivalent (von Mises) stress showed a 27.5% enhancement under downpull conditions. Stress concentration patterns remained consistent, predominantly occurring at geometric discontinuities where elevated stress levels do not necessarily indicate impending failure. However, comparative analysis confirmed the End Vertical Girder consistently experiences higher load demands than the Main Horizontal Beams, reinforcing its function as the principal load-bearing structural element.

Transient deformation analysis revealed characteristic damped oscillatory behavior throughout the 2-second simulation period for both loading scenarios. The inclusion of downpull forces produced a marginal increase in peak deformation magnitudes. The study findings emphasize the critical importance of incorporating downpull effects in the design process to ensure structural longevity and prevent potential fatigue-related issues. Such comprehensive analysis enables optimized structural performance and enhanced operational reliability of hydraulic gate systems.

5.2 Recommendation

This research focuses on the numerical and analytical calculation of downpull. To further investigate the effects of hydrodynamic forces on various gate lips and openings, a physical model of the structure can be developed for experimental studies.

Future research could also explore material enhancements and alternative gate geometries to minimize the adverse impact of hydrodynamic forces.

REFERENCES

Bilal Ahmed, D. M. (2022). Finite Element analysis of a portable Sluice Gate for NVDA Malwa region, India (M.P). *International Journal of Advances in Engineering and Management (IJAEM), 4*(7), 232-240.

Erbisti, P. C. (2014). *Design of Hydraulic Gates.* London, UK: CPI Group Ltd.

Escobar, J. C. (2018). *Analysis of Hydrodynamic Forces on High-Head Slide Gates Using CFD.* Medellín, Colombia : Universidad Nacional de Colombia.

Hao Zhe Khor, H. T. (2023). Influence of Gate Lip Angle on Downpull Forces for Vertical Lift Gate. *IOP Conf. Series: Earth and Environmental Science.* San Francisco, CA.

MAGNUSSON, M. S. (2014). *Numerical study on hydraulic vertical gate.* STOCKHOLM, SWEDEN: KTH ROYAL INSTITUTE OF TECHNOLOGY.

UYSAL, M. A. (2014). *PREDICTION OF DOWNPULL ON HIGH HEAD GATES USING CFD.* Middle East Technical University.

Wahab, M. A. (2005). *Stress Analysis of Fixed Wheel Vertical-Lift Gate by Finite Element Method.* Roorkee, India: Department of Water Resource Development and Management, IIT Roorkee.

APPENDICES

APPENDIX A: Analytical Calculation for Downpull Force

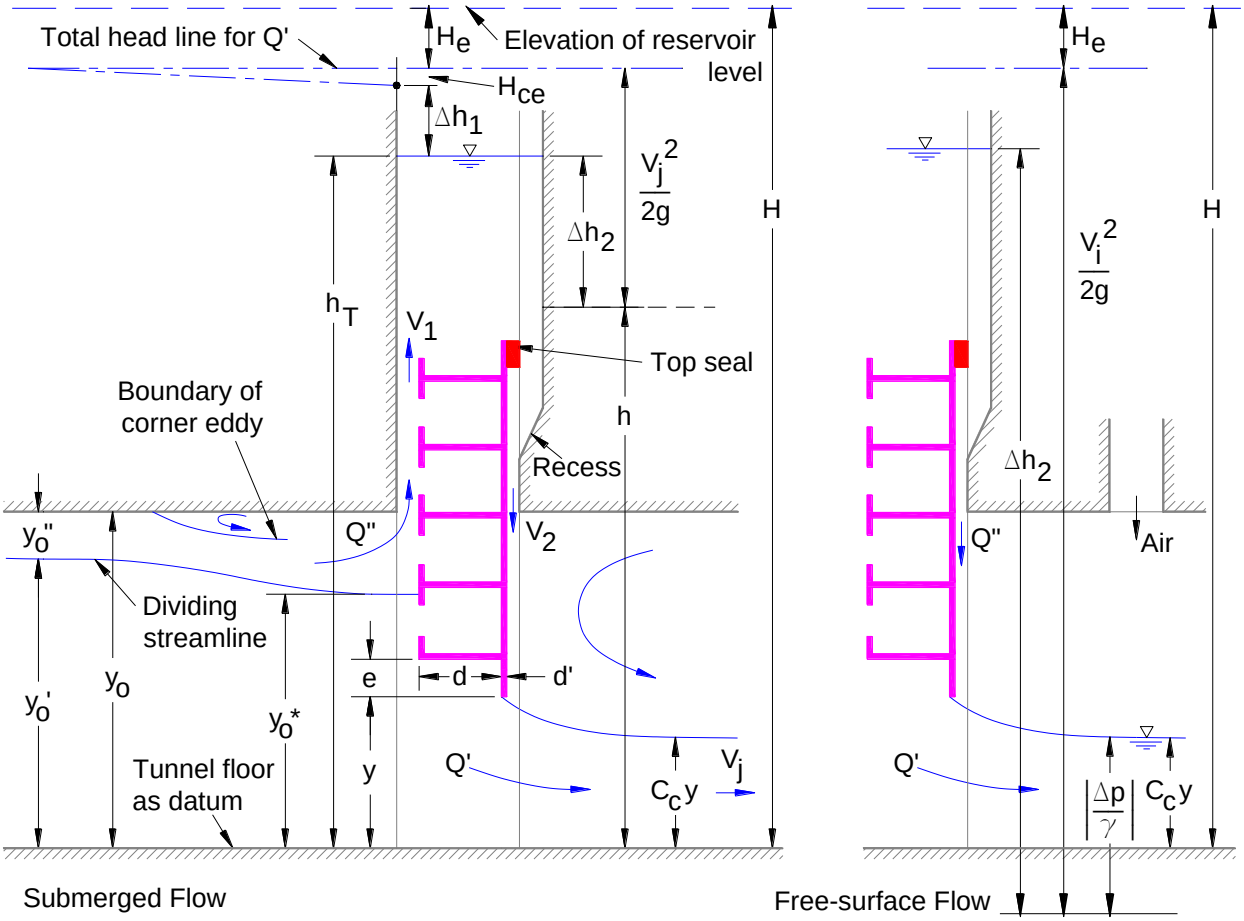

Gate location		Tunnel	
Gate bottom angle	θ	25	deg
Bottom lip ratio	e/d	0.3	
Lintel seal protrusion	a2	0.600	cm
Clearance upstream of gate	a1	1.100	cm
Recess depth	a"2	0.600	cm
Maximum total flow	Q	20,940,000.00	cms
Gate thickness	d	0.210	m
Lead-in radius ratio	r/d	0.0	
Bottom lip projection	e	0.000	cm
Height of tunnel	yo	1.500	m
Projection area of top seal	As	126.600	cm^2
a"2/(a2+a"2)		0.500	
Flow coefficient over gate	C2	0.657	
Tunnel area	Ao	3.17	m^2

Gate opening ratio	x	10%	20%	30%	40%	50%	80%	
Gate opening	y	0.2	0.3	0.5	0.6	0.8	1.2	m
Contraction coefficient	Cc	0.730	0.732	0.736	0.743	0.753	0.804	
Bottom Downpull coefficient	κB	**0.613**	**0.293**	**0.124**	**0.077**	**0.099**	**0.410**	
Downstream head	h	0.109	0.220	0.331	0.446	0.565	0.965	m
Discharge jet velocity	Vj	16.74	16.68	16.61	16.54	16.47	16.23	m/s
Discharge under the gate	Q'	3.87	7.73	11.61	15.56	19.63	33.05	cms
Flow coefficient over gate	C1	0.850	0.816	0.786	0.760	0.736	0.675	
Discharge at lintel	Q"	0.13	0.13	0.12	0.12	0.12	0.10	cms
	κT'	0.997	0.988	0.975	0.953	0.924	0.752	
Top Downpull coefficient	κT	0.846	0.829	0.807	0.779	0.747	0.587	
	Δh2	12.090	11.752	11.354	10.877	10.333	7.882	m
Total flow	Q	4.00	7.85	11.73	15.68	19.74	33.15	cms
Approach velocity	Vo	1.26	2.48	3.71	4.96	6.24	10.47	m/s
Corner eddy head loss	Hce	0.056	0.175	0.372	0.667	1.062	3.351	m
	Δh1	2.144	2.254	2.342	2.410	2.440	2.202	m
Head in gate well	hT	12.200	11.971	11.686	11.323	10.898	8.847	m
DOWNPULL COMPONENT								
pressure difference between top and bottom surfaces of the gate	F1	14,452	33,024	41,739	42,578	38,927	10,332	N
pressure difference acting on the extended skin plate	F2	2,502	2,432	2,349	2,251	2,138	1,631	N
lintel seal protrusion at the top of the gate	F3	0	0	0	0	0	0	N
Total Downpull	**F**	**16,954**	**35,456**	**44,088**	**44,829**	**41,065**	**11,963**	**N**

APPENDIX B: Gate Design

1	**Design data:**				
	Gate opening width	w	=	2.00	m
	Gate opening height	h	=	1.50	m
	Design head	H	=	10.67	m
	Seal span	B	=	2.10	m
	Roller span	L	=	2.20	m
	Density of water	γ	=	1.00	
	Young's Modulus of elasticity of steel	E	=	200,000.00	N/mm^2
2	**Design load:**			-	
	Height of water above top of gate	X	=	9.17	m
	Total Water Load on gate	W	=	31.25	kN
3	**Main horizontal beam arrangement:**			-	
	Thickness of skin plate	t	=	10.00	mm
	Ultimate tensile stress of steel of beam	UTS	=	410.00	N/mm^2
	Water head wrt gate centre	H_m	=	9.92	m
	Yield stress	f_y	=	250.00	N/mm^2
	Allowable bending stress	σ_{all}	=	112.50	N/mm^2
	Number of horizontal beam required		=	3.15	
	*100*h*sqrt(H $_m$)//(t*sqrt(2* σ $_{all}$))*			-	
	Provide No of beams	n	=	4.00	
	β=n(H-h)^2/{H^2-(H-h)^2}*		=	11.30	
	Numbering of Beam from Top		=	k	
	Calculated Position of beam from water level		=	y_{kc}	
	*y $_k$ =2*H[(k+β)^(1.5)-(k-1+β)^(1.5)]/{3*(n+β)^0.5}*				
	Provided position of beam from water level		=	y_{kp}	
	Spacing of Beam		=	s_{HB}	
	Water Load on Beam		=	W_k	

k	y_{kc}	y_{kp}	s_{HB}	γ*y	W_k
	m	m	m	ton/m^2	ton
1	9.37	9.17	0.59	9.17	5.80
2	9.76	9.76	0.37	9.76	9.76
3	10.13	10.13	0.36	10.13	7.76
4	10.49	10.49	0.18	10.49	7.92
Gate Bottom		10.67		10.67	
				Total	**31.25**

Horizontal Beam Design

1	**Beam No.**			**1**		
2	Location of beam wrt water level		=	9.17	m	
3	BM	M_{max}	=	1.67	tm	
4	SF(Smax)	S_{max}	=	2.90	t	
5	Section		=	ISMB250		
6	Moment of inertia(I)	I	=	5,131.60	cm^4	
7	Section modulus(Z)	Z	=	410.53	cm^4	
8	Sectional area(Aw)	A_w	=	47.55	cm^2	
9	Overall depth of beam(D)	D	=	250.00	mm	
10	Thickness of flange(tf)	t_f	=	12.50	mm	
11	Thickness of web(tw)	t_w	=	6.90	mm	
12	radius of gyration(yy)	γ_y	=	26.52	mm	
13	Ultimate tensile stress of steel	UTS	=	410.00	N/mm^2	
14	Yield stress(fy)	F_y	=	250.00	N/mm^2	IS 800:2007 / Table1
15	Bending stress in beam	σ_{max}	=	39.86	N/mm^2	
16	Allowable bending stress	σ_{all}	=	112.50	N/mm^2	IS 4622:2003 / ANNEX B
17	Check for bending stress			safe		
18	Shear stress in beam	τ_{max}	=	5.99	N/mm^2	
19	Allowable shear stress	τ_{all}	=	87.50	N/mm^2	IS 4622:2003 / ANNEX B
20	Check for shear stress			safe		
21	Deflection	Y_{max}	=	0.80	mm	
22	Check for deflection			safe		IS 4622:2003 / cl5.3.5
1	**Beam No.**			**2**		
2	Location of beam wrt water level		=	9.76	m	
3	BM	M_{max}	=	2.81	tm	
4	SF(Smax)	S_{max}	=	4.88	t	
5	Section		=	ISMB250		
6	Moment of inertia(I)	I	=	5,131.60	cm^4	
7	Section modulus(Z)	Z	=	410.53	cm^4	
8	Sectional area(Aw)	A_w	=	47.55	cm^2	
9	Overall depth of beam(D)	D	=	250.00	mm	
10	Thickness of flange(tf)	t_f	=	12.50	mm	
11	Thickness of web(tw)	t_w	=	6.90	mm	
12	radius of gyration(yy)	γ_y	=	26.52	mm	
13	Ultimate tensile stress of steel	UTS	=	410.00	N/mm^2	
14	Yield stress(fy)	F_y	=	250.00	N/mm^2	IS 800:2007 / Table1
15	Bending stress in beam	σ_{max}	=	67.08	N/mm^2	
16	Allowable bending stress	σ_{all}	=	112.50	N/mm^2	IS 4622:2003 / ANNEX B
17	Check for bending stress			safe		
18	Shear stress in beam	τ_{max}	=	10.07	N/mm^2	
19	Allowable shear stress	τ_{all}	=	87.50	N/mm^2	IS 4622:2003 / ANNEX B
20	Check for shear stress			safe		
21	Deflection	Y_{max}	=	1.35	mm	
22	Check for deflection			safe		IS 4622:2003 / cl5.3.5
1	**Beam No.**			**3**		
2	Location of beam wrt water level		=	10.13	m	
3	BM	M_{max}	=	2.23	tm	

Horizontal Beam Design

4	SF(Smax)	S_{max}	=	3.88	t	
5	Section		=	ISMB250		
6	Moment of inertia(I)	I	=	5,131.60	cm^4	
7	Section modulus(Z)	Z	=	410.53	cm^4	
8	Sectional area(Aw)	A_w	=	47.55	cm^2	
9	Overall depth of beam(D)	D	=	250.00	mm	
10	Thickness of flange(tf)	t_f	=	12.50	mm	
11	Thickness of web(tw)	t_w	=	6.90	mm	
12	radius of gyration(γy)	γ_y	=	26.52	mm	
13	Ultimate tensile stress of steel	UTS	=	410.00	N/mm^2	
14	Yield stress(fy)	F_y	=	250.00	N/mm^2	IS 800:2007 / Table1
15	Bending stress in beam	σ_{max}	=	53.33	N/mm^2	
16	Allowable bending stress	σ_{all}	=	112.50	N/mm^2	IS 4622:2003 / ANNEX B
17	Check for bending stress			safe		
18	Shear stress in beam	τ_{max}	=	8.01	N/mm^2	
19	Allowable shear stress	τ_{all}	=	87.50	N/mm^2	IS 4622:2003 / ANNEX B
20	Check for shear stress			safe		
21	Deflection	Y_{max}	=	1.07	mm	
22	Check for deflection			safe		IS 4622:2003 / cl5.3.5

1	**Beam No.**			**4**		
2	Location of beam wrt water level		=	10.49	m	
3	BM	M_{max}	=	2.28	tm	
4	SF(Smax)	S_{max}	=	3.96	t	
5	Section		=	ISMB250		
6	Moment of inertia(I)	I	=	5,131.60	cm^4	
7	Section modulus(Z)	Z	=	410.53	cm^4	
8	Sectional area(Aw)	A_w	=	47.55	cm^2	
9	Overall depth of beam(D)	D	=	250.00	mm	
10	Thickness of flange(tf)	t_f	=	12.50	mm	
11	Thickness of web(tw)	t_w	=	6.90	mm	
12	radius of gyration(γy)	γ_y	=	26.52	mm	
13	Ultimate tensile stress of steel	UTS	=	410.00	N/mm^2	
14	Yield stress(fy)	F_y	=	250.00	N/mm^2	IS 800:2007 / Table1
15	Bending stress in beam	σ_{max}	=	54.41	N/mm^2	
16	Allowable bending stress	σ_{all}	=	112.50	N/mm^2	IS 4622:2003 / ANNEX B
17	Check for bending stress			safe		
18	Shear stress in beam	τ_{max}	=	8.17	N/mm^2	
19	Allowable shear stress	τ_{all}	=	87.50	N/mm^2	IS 4622:2003 / ANNEX B
20	Check for shear stress			safe		
21	Deflection	Y_{max}	=	1.10	mm	
22	Check for deflection			safe		IS 4622:2003 / cl5.3.5

Side Vertical Grider Design

	Roller 1	Roller 2
Position of roller from top	0.38	1.05
Reaction on	7.81	7.81

Beam	Height difference	Forces	Bending moment	Shear force
	(m)	(ton)	(ton m)	(ton)
1	0	2.90	0	2.90
reaction	0.38	4.88	1.10	7.78
2	0.03	-7.81	1.34	-0.03
3	0.40	3.88	1.32	3.85
reaction	0.24	-7.81	2.25	-3.96
4	0.12	3.30	1.77	-0.66
bottom	0.18	0.00	1.66	-0.66

Section	ISMC 250		
Weight per Meter (w)		30.4	kg/m
Sectional Area (a)		38.67	cm^2
Depth of Section (h)		250	mm
Width of flange (b)		80	mm
Thickness of Flange (tf)		14.1	mm
Thickness of Web (tw)		7.1	mm
Moment of Inertia	Ixx	3816.8	cm^4
	Iyy cm4	219.1	cm^4
Raddi of Gyration	rxx cm	9.94	cm
	ryy cm	2.38	cm
Modulli of Section	Zxx cm3	305.3	cm^3
	Zyy cm3	38.4	cm^3
Centre of Gravity	Cxx	7.1	cm

Maximum bending moment	BMmax	2.25	tm
Shear Force	S.Fmax	7.78	t
Section modulus (req)	Zreq	196.13	cm^3
Bending stress	(112.5)N/mm^2	72.27	N/mm^2
Shear Force	(87.5)N/mm^2	19.75	N/mm^2
Equivalent Stress	(112.5)N/mm^2	79.95	N/mm^2

APPENDIX C: Analytical Calculation of Equivalent Stress

Beam number	Bending stress	Shear stress	Equivalent Stress (Without Downpull)
	(112.5)N/mm^2	(87.5)N/mm^2	(112.5)N/mm^2
1	39.87	5.99	41.19
2	67.09	10.07	69.32
3	53.33	8.01	55.10
4	54.41	8.17	56.22

Side Vertical Grider Design

Section	ISMC 250		
Weight per Meter (w)		30.4	kg/m
Sectional Area (a)		38.67	cm^2
Depth of Section (h)		250	mm
Width of flange (b)		80	mm
Thickness of Flange (tf)		14.1	mm
Thickness of Web (tw)		7.1	mm
Moment of Inertia	Ixx	3816.8	cm^4
	Iyy cm4	219.1	cm^4
Raddi of Gyration	rxx cm	9.94	cm
	ryy cm	2.38	cm
Modulli of Section	Zxx cm3	305.3	cm^3
	Zyy cm3	38.4	cm^3
Centre of Gravity	Cxx	7.1	cm
Maximum bending moment	BMmax	2.25	tm
Shear Force	S.Fmax	7.78	t
Section modulus (req)	Zreq	196.13	cm^3
Bending stress	(112.5)N/mm^2	72.27	N/mm^2
Shear Force	(87.5)N/mm^2	19.75	N/mm^2
Equivalent Stress	(112.5)N/mm^2	79.95	N/mm^2

Beam number	Bending stress	Shear stress	Equivalent Stress (With Downpull)
	(112.5)N/mm^2	(87.5)N/mm^2	(112.5)N/mm^2
1	40.76	6.12	42.11
2	67.62	10.15	69.87
3	54.00	8.11	55.80
4	55.07	8.27	56.90

Side Vertical Grider Design (With Downpull)

Section	ISMC 250		
Weight per Meter (w)		30.4	kg/m
Sectional Area (a)		38.67	cm^2
Depth of Section (h)		250	mm
Width of flange (b)		80	mm
Thickness of Flange (tf)		14.1	mm
Thickness of Web (tw)		7.1	mm
Moment of Inertia	Ixx	3816.8	cm^4
	Iyy cm4	219.1	cm^4
Raddi of Gyration	rxx cm	9.94	cm
	ryy cm	2.38	cm
Modulli of Section	Zxx cm3	305.3	cm^3
	Zyy cm3	38.4	cm^3
Centre of Gravity	Cxx	7.1	cm
Maximum bending moment	BMmax	2.35	tm
Shear Force	S.Fmax	7.89	t
Section modulus (req)	Zreq	205.35	cm^3
Bending stress	(112.5)N/mm^2	75.67	N/mm^2
Shear Force	(87.5)N/mm^2	20.01	N/mm^2
Equivalent Stress	(112.5)N/mm^2	83.23	N/mm^2

APPENDIX D: Letter of Paper Acceptance at IOEGC

Gmail — Ranjeet Twayna <ranjeet.twayna@gmail.com>

[IOEGC16] Editor Decision
1 message

Kobid <conference-noreply@ioe.edu.np> Mon, Mar 31, 2025 at 12:07 PM
To: Ranjeet Twayna <ranjeet.twayna@gmail.com>

Ranjeet Twayna, Laxman Poudel:

We are pleased to inform you that your manuscript titled "Hydrodynamic Forces and their Effect on Structural Design of Vertical Lift Gate" submitted to 16th IOE Graduate Conference is **Accepted** for presentation in the Conference as well as inclusion in the Peer-Reviewed Proceedings.
Please note that inclusion in hard copy proceedings is contingent upon your timely response to further edits, if any, during the publication process.

With Warm Regards,
IOEGC-16 Editorial Team

APPENDIX E: Similarity Report

Ranjeet Twayna

Hydrodynamic Forces and their Effects on Structural Design of Vertical Lift Gate

Tribhuvan University

Document Details

Submission ID
trn:oid:::3117:449961836

Submission Date
Apr 17, 2025, 5:02 PM GMT+5:45

Download Date
Apr 17, 2025, 5:04 PM GMT+5:45

File Name
Plag check.docx

File Size
3.6 MB

60 Pages

8,574 Words

48,278 Characters

iThenticate Page 1 of 65 - Cover Page Submission ID trn:oid:::3117:449961836

9% Overall Similarity

The combined total of all matches, including overlapping sources, for each database.

Filtered from the Report

- Bibliography
- Quoted Text
- Cited Text
- Small Matches (less than 8 words)

Match Groups

67 Not Cited or Quoted 9%
Matches with neither in-text citation nor quotation marks

0 Missing Quotations 0%
Matches that are still very similar to source material

0 Missing Citation 0%
Matches that have quotation marks, but no in-text citation

0 Cited and Quoted 0%
Matches with in-text citation present, but no quotation marks

Top Sources

6% Internet sources
7% Publications
0% Submitted works (Student Papers)

Integrity Flags

1 Integrity Flag for Review

Replaced Characters
30 suspect characters on 4 pages
Letters are swapped with similar characters from another alphabet.

Our system's algorithms look deeply at a document for any inconsistencies that would set it apart from a normal submission. If we notice something strange, we flag it for you to review.

A Flag is not necessarily an indicator of a problem. However, we'd recommend you focus your attention there for further review.

iThenticate Page 2 of 65 - Integrity Overview Submission ID trn:oid:::3117:449961836

Match Groups

- 67 Not Cited or Quoted 9%
  Matches with neither in-text citation nor quotation marks
- 0 Missing Quotations 0%
  Matches that are still very similar to source material
- 0 Missing Citation 0%
  Matches that have quotation marks, but no in-text citation
- 0 Cited and Quoted 0%
  Matches with in-text citation present, but no quotation marks

Top Sources

6% Internet sources
7% Publications
0% Submitted works (Student Papers)

Top Sources

The sources with the highest number of matches within the submission. Overlapping sources will not be displayed.

1	Publication	Paulo C.F. Erbisti. "Design of Hydraulic Gates", CRC Press, 2019 — 1%
2	Internet	www.slideshare.net — 1%
3	Internet	bdigital.unal.edu.co — <1%
4	Publication	Hao Zhe Khor, How Tion Puay. "Influence of Gate Lip Angle on Downpull Forces fo... — <1%
5	Publication	Juan C. Arango Escobar, David Calderon Villegas, Aldo Benavides Moran, Alejandr... — <1%
6	Internet	oa.doria.fi — <1%
7	Internet	repository.ju.edu.et — <1%
8	Internet	digitalcommons.usf.edu — <1%
9	Internet	eprints.utas.edu.au — <1%
10	Publication	Xiang Zou, Liandong Fu, Lin Wu, Wenhao Zuo. "Research on Multiphase Flow and ... — <1%

iThenticate Page 3 of 65 - Integrity Overview Submission ID trn:oid:::3117:449961836